

This work was written as part of one of the author's official duties as an Employee of the United States Government and is therefore a work of the United States Government. In accordance with 17 U.S.C. 105, no copyright protection is available for such works under U.S. Law.

Public Domain Mark 1.0

<https://creativecommons.org/publicdomain/mark/1.0/>

Access to this work was provided by the University of Maryland, Baltimore County (UMBC) ScholarWorks@UMBC digital repository on the Maryland Shared Open Access (MD-SOAR) platform.

Please provide feedback

Please support the ScholarWorks@UMBC repository by emailing scholarworks-group@umbc.edu and telling us what having access to this work means to you and why it's important to you. Thank you.

The Sensitivity of SeaWiFS Ocean Color Retrievals to Aerosol Amount and Type

RALPH A. KAHN

Earth Science Division, NASA Goddard Space Flight Center, Greenbelt, Maryland

ANDREW M. SAYER

Earth Science Division, NASA Goddard Space Flight Center, Greenbelt, and Goddard Earth Sciences Technology and Research, Universities Space Research Association, Columbia, Maryland

ZIAUDDIN AHMAD

Earth Science Division, NASA Goddard Space Flight Center, Greenbelt, and Science and Data Systems, Inc., Silver Spring, Maryland

BRYAN A. FRANZ

Earth Science Division, NASA Goddard Space Flight Center, Greenbelt, Maryland

(Manuscript received 2 June 2015, in final form 14 March 2016)

ABSTRACT

As atmospheric reflectance dominates top-of-the-atmosphere radiance over ocean, atmospheric correction is a critical component of ocean color retrievals. This paper explores the operational Sea-viewing Wide Field-of-view Sensor (SeaWiFS) algorithm atmospheric correction with $\sim 13\,000$ coincident surface-based aerosol measurements. Aerosol optical depth at 440 nm (AOD_{440}) is overestimated for AOD below ~ 0.1 – 0.15 and is increasingly underestimated at higher AOD; also, single-scattering albedo (SSA) appears overestimated when the actual value $< \sim 0.96$. AOD_{440} and its spectral slope tend to be overestimated preferentially for coarse-mode particles. Sensitivity analysis shows that changes in these factors lead to systematic differences in derived ocean water-leaving reflectance (R_{rs}) at 440 nm. The standard SeaWiFS algorithm compensates for AOD anomalies in the presence of nonabsorbing, medium-size-dominated aerosols. However, at low AOD and with absorbing aerosols, in situ observations and previous case studies demonstrate that retrieved R_{rs} is sensitive to spectral AOD and possibly also SSA anomalies. Stratifying the dataset by aerosol-type proxies shows the dependence of the AOD anomaly and resulting R_{rs} patterns on aerosol type, though the correlation with the SSA anomaly is too subtle to be quantified with these data. Retrieved chlorophyll-*a* concentrations (Chl) are affected in a complex way by R_{rs} differences, and these effects occur preferentially at high and low Chl values. Absorbing aerosol effects are likely to be most important over biologically productive waters near coasts and along major aerosol transport pathways. These results suggest that future ocean color spacecraft missions aiming to cover the range of naturally occurring and anthropogenic aerosols, especially at wavelengths shorter than 440 nm, will require better aerosol amount and type constraints.

1. Introduction

Ocean color refers to the spectral distribution of visible radiance upwelling from below the ocean surface. It carries information about the optically active

constituents in the euphotic zone of the upper ocean, such as the concentration of the phytoplankton pigment chlorophyll-*a*. The physical quantity is expressed in terms of water-leaving radiance [L_w ($\text{W m}^{-2} \text{sr}^{-1} \mu\text{m}^{-1}$)] or remote sensing reflectance [R_{rs} (sr^{-1})]; the latter is obtained from the former by correcting for bidirectional effects of the air–sea interface and inhomogeneity of the subsurface light field (Morel et al. 2002), and then dividing by $E_d(0+)$, the downwelling irradiance just above the sea surface (Wang 2010). [Formally, $E_d(0+) = \mu_0 F_{0\downarrow 0}$,

Corresponding author address: Ralph A. Kahn, Earth Science Division, NASA Goddard Space Flight Center, Mail Code 613, Greenbelt, MD 20771.
E-mail: ralph.kahn@nasa.gov

where μ_0 is the cosine of the solar zenith angle, F_0 is the instantaneous extraterrestrial solar irradiance, and t_0 is the atmospheric diffuse transmittance from the sun to the surface.] Retrieval of R_{rs} from space-based observations requires that atmospheric and other surface contributions to the observed radiance at the top of the atmosphere (TOA) be identified and removed, including those from scattering and absorption by airborne particles. This issue is well known; typically 85%–90% of the TOA signal over ocean at midvisible and shorter wavelengths, critical to ocean color science, actually comes from scattering by air molecules and aerosols that comprise the overlying atmosphere, necessitating a high-quality “atmospheric correction” to retrieve L_w (e.g., [Gordon and Wang 1994](#)). The basic atmospheric correction approach adopted by NASA’s Ocean Biology Processing Group (OBPG) for the Sea-viewing Wide Field-of-view Sensor (SeaWiFS; [McClain et al. 1998](#)) and Moderate Resolution Imaging Spectroradiometer (MODIS; [Esaias et al. 1998](#)) amounts to constraining aerosol optical depth (AOD) and aerosol type over dark (case 1; [Morel and Prieur 1977](#)) waters, based on a pair of near-infrared (NIR) channels, where the ocean surface tends to be dark (765- and 865-nm band centers for SeaWiFS; 748 and 869 nm for MODIS). Using the AOD and selected aerosol models, AOD and absorbing AOD [AAOD, defined as $AOD \times (1 - SSA)$, where SSA is the single-scattering albedo, are extrapolated to green and blue wavelengths, where the atmospheric correction must be applied for the ocean color analysis ([Gordon and Wang 1994](#); [Gordon 1997](#); [Ahmad et al. 2010](#)). (Note that although the key SeaWiFS band centers for most of this study are at 443 and 865 nm, for discussion purposes we refer to them as 440 and 870 nm, respectively in most cases.)

To minimize systematic bias in the L_w retrievals, considering both errors in instrument calibration and the atmospheric correction process, the OBPG developed a vicarious calibration procedure ([Franz et al. 2007](#)). The calibration of the longest NIR band is assumed correct, and the shortest NIR band is adjusted so the aerosol-type retrieval in the South Pacific gyre agrees, on average over the mission life span, with in situ measurements from the Aerosol Robotic Network (AERONET; [Holben et al. 1998](#)) site located in Tahiti. With the NIR calibration fixed, the visible-band calibration is then adjusted to force mission-average agreement with water-leaving radiances measured by the Marine Optical Buoy (MOBY) offshore near Lanai, Hawaii ([Clark et al. 1997](#)). The resulting vicarious calibration coefficients are then applied globally. In effect, the combined instrument calibration and tuned atmospheric correction are optimized for best performance over Lanai or other locations having similar environmental conditions.

For the atmospheric correction process to work generally, the AOD itself, and the differences in the AOD and AAOD spectral *slopes* among the aerosol types that are in the field of view, must be taken into account (e.g., [Ahmad et al. 2010](#)), because the correction effectively constrains the short-wave reflectance based upon both the AOD magnitude at the longer wavelengths and the spectral ratios of particle scattering and absorption properties from the NIR to the blue. Over open ocean, away from continental aerosol source regions and transported aerosol plumes, typical midvisible AOD is in the range 0.05–0.12 ([Smirnov et al. 2011](#)). Near many coasts, and under spatially extensive plumes quite far downwind of major sources, midvisible AOD can reach 0.35 or more over large ocean areas ([Remer et al. 2008](#); [Colarco et al. 2014](#)). Some examples of regions where AOD can be large, and aerosol contributions to TOA reflectance can be significant and highly variable, include the North Atlantic downwind of the Sahara Desert, especially during northern spring and much of summer as far west as the Caribbean; the equatorial and South Atlantic during their respective burning seasons in sub-Saharan, central, and southern Africa; the Arabian Gulf, the Black and Caspian Seas, and the Mediterranean, especially during spring and summer; the western Pacific during the spring dust season, the winter pollution season, and biomass burning episodes; and the Bay of Bengal during winter and premonsoon (e.g., [Kinne et al. 2006](#); [Huang et al. 2010](#); [Kalashnikova and Kahn 2008](#); [Remer et al. 2008](#); [Smirnov et al. 2002, 2011](#)).

Among the aerosol types that dominate at different locations and in different seasons over ocean are Saharan dust; Gobi Desert dust; different types of organic (“brown”) carbon, such as most wildfire smoke and some urban pollution particles; black carbon (e.g., from diesel and some fire combustion products); and background sea-salt and sulfate particles. The microphysical properties of these particles vary considerably. Some scatter but do not absorb visible light, such as sulfates and sea salt, whereas biomass burning smoke, other organic carbon components, and desert dusts absorb more heavily, though to varying degrees, toward shorter visible and ultraviolet (UV) wavelengths, and some pollution aerosols absorb heavily across the entire visible spectrum and into the UV. Most importantly for the atmospheric correction procedure, the spectral slopes of aerosol scattering and absorption vary in both magnitude and sign, depending on aerosol type, with dusts typically scattering more efficiently at longer visible wavelengths, but smoke and pollution particles scattering more efficiently at shorter wavelengths (e.g., [Dubovik et al. 2002](#); [Smirnov et al. 2002](#); [Eck et al. 2003, 2005](#); [Ahmad et al. 2010](#); [Russell et al. 2010](#)).

A number of previous studies have explored the challenge of accounting specifically for aerosol type in ocean color atmospheric correction. Most of these studies focused on the influence of blue-absorbing aerosols, because if they are present but unaccounted for, the retrieval algorithm will overestimate the atmospheric contribution to TOA reflectance toward the blue and retrieve underestimated or even negative surface reflectances at the shorter wavelengths. (Note that the most common light-absorbing particles, such as desert dust, wildfire smoke, and pollution particles, absorb in the blue, but to varying degrees, and with varying spectral dependence.) For example, [Li et al. \(2003\)](#) analyzed three events during the Asian Pacific Regional Aerosol Characterization Experiment (ACE-Asia) field campaign when shipboard aerosol measurements were acquired in the East China Sea and the Sea of Japan, coincident with SeaWiFS overpasses. Different combinations of absorbing aerosol optical analogs, fine-mode pollution particles, and coarse-mode Asian mineral dust, plus nonabsorbing sea salt, were required to reproduce the surface and TOA reflectances to within experimental accuracy. They also showed that assuming a fixed aerosol mixture, even of the three components measured in situ, would not produce satisfactory L_w results for this region and season (local spring). [Schollaert et al. \(2003\)](#) identified similar issues over the case 1 waters of the western North Atlantic off the U.S. East Coast, where background sulfate and Saharan Desert dust particles are found in amounts and proportions that vary with season and location. Atmospheric absorption was underestimated toward shorter wavelengths in the presence of the dust, and sulfate particles caused the magnitude of the negative green-to-blue AOD spectral slope to increase, in both cases skewing the blue-to-green ratio of L_w values derived from the SeaWiFS operational Data Analysis System (SeaDAS) low, consequently overestimating the chlorophyll-*a* absorption and therefore its retrieved concentration.

[Ransibrahmanakul and Stumpf \(2006\)](#) attempted to partly compensate empirically for unduly large SeaWiFS short-wavelength atmospheric correction by assuming an aerosol optical model having spectral absorption containing artifacts that vary as λ^{-6} , where λ is the wavelength. Assuming atmospheric absorption is negligible at 670 nm and that the ratio of actual ocean reflectance to that obtained from a retrieval “contaminated” by absorbing aerosol between 510- and 670-nm wavelength is spectrally invariant, and knowing the spectral dependence of chlorophyll absorption, they derive an adjusted short-wave aerosol absorption contribution. As they point out, this procedure works only to the extent that the aerosol optical model used provides a fair representation of the aerosols actually present, which

requires external constraints on aerosol type that are generally unavailable from current sources.

Depending on the aerosol type, the spectral dependence of aerosol scattering and absorption can also produce *smaller* TOA aerosol reflectance at shorter wavelengths than the extrapolated values. If this effect is uncorrected, it can cause an overestimate of surface reflectance—so the retrieved chlorophyll concentration, based on its short-wave absorption, would be underestimated. However, the result is less likely to be clearly unphysical, as it is when uncorrected aerosol absorption produces negative surface reflectances. [Porter and Nielsen \(2002\)](#) highlighted this issue for the special case of a volcanic plume over the ocean near Hawaii. They demonstrate that increased scattering toward shorter wavelengths, characteristic of volcanic aerosol particles compared to the aerosol model assumed in an early version of the SeaDAS processing, produced a high bias of as much as ~40% in the water-leaving radiance.

[Nobileau and Antoine \(2005\)](#) also recognized that underestimating the scattering versus absorbing effects of aerosols in the blue ocean color bands can produce underestimates or overestimates of L_w . They demonstrate a retrieval using the NIR bands to identify a candidate nonabsorbing maritime aerosol, as with the standard methods, but then compare the implied TOA reflectance at 510 nm with that observed. This wavelength represents an approximate neutral point for the long-wave scattering and short-wave absorption behavior of typical ocean surface material in case 1 waters, so the contribution to L_w , and hence its absolute uncertainty, is minimized; if the derived TOA reflectance exceeds the observed value beyond some threshold, absorbing aerosol is inferred.

[Nobileau and Antoine \(2005\)](#) developed and tested the algorithm for Saharan dust optical analogs. Desert dust is among the most abundant aerosol types in global average, and specifically in the regions they studied. Although they recognized that carbonaceous smoke or pollution particles dominate over ocean at some places and times, distinguishing the unique spectral absorption of these aerosol types, as distinct from desert dust, was beyond the scope of their study, as was refining the AOD spectral dependence of the standard scattering-aerosol optical models. [Antoine and Nobileau \(2006\)](#) then applied this technique as a method for actual aerosol retrieval, based on 7 years of SeaWiFS data over the Mediterranean, using time-dependent rather than fixed values for the marine reflectance and its standard deviation at 510 nm. They interpret low Ångström exponent (i.e., large size), absorbing particles as African dust, augmenting the background maritime aerosol, though they do not explore the implications of these results as an atmospheric correction for ocean color applications.

Despite extensive analysis of atmospheric correction in individual cases where absorbing aerosols dominate, the global distribution of regional and temporal situations where the derived chlorophyll-*a* concentration is unduly small—for example, because of uncorrected aerosol scattering—has not been studied explicitly. [Ahmad et al. \(2010\)](#) developed an advanced set of 80 aerosol optical models for the SeaWiFS and MODIS atmospheric corrections, obtained primarily from a global climatology of aerosol properties as derived from AERONET surface-based sun- and sky-scanning photometer measurements ([Holben et al. 1998](#)). These include optical models for commonly occurring aerosol types having a much broader range of absorbing and scattering properties than earlier versions of the retrieval algorithm, keyed to 10 different fine-to-coarse-mode ratios and eight relative humidity (RH) values.

Yet the aerosol type selected and the short-wave AOD derived by the operational algorithms for atmospheric correction in a given retrieval situation is still determined primarily by band ratios between two NIR observations. Prior to the implementation of the [Ahmad et al. \(2010\)](#) advanced aerosol optical models, the aerosol types employed by the SeaWiFS and MODIS algorithms produced AOD spectral slopes [parameterized as the Ångström exponent (ANG)] that were significantly underestimated relative to coincident AERONET observations, indicating the need for improved aerosol models ([Mélin et al. 2010](#); [Mélin and Zibordi 2010](#)). Subsequent evaluation of the algorithms, with the advanced particle models applied, demonstrated that these models improved both the AOD and ANG relative to AERONET over much of the range of observing geometries ([He et al. 2011](#); [Mélin et al. 2013a,b](#)). These papers also highlighted the importance of correctly representing the aerosol single-scattering phase function (discussed further in [section 2c](#) below), and of the atmospheric correction in general for ocean color retrieval.

Several other recent studies also make use of AERONET data to assess or improve upon atmospheric correction for ocean color applications. [Aznay et al. \(2014\)](#) evaluated the European Space Agency's Medium Resolution Imaging Spectrometer (MERIS) atmospheric correction process with coincident observations from the Venice, Italy, AERONET site. The study determined that the atmospheric reflectance at 412 nm had been overestimated, producing an underestimate of the ocean reflectance and a significant overestimate of algal pigment indices, but reserved for future work an analysis that accounts for the impact of different aerosol types on the results. [McCarthy et al. \(2012\)](#) looked at aerosol model selection for the MODIS atmospheric correction, in the context of AERONET ocean color (AERONET-OC)

observations of both AOD and L_w at three sites where such data were collected: Venice, Martha's Vineyard, and the Gulf of Mexico. For the 93 cases included, they attempted to identify an "optimal" model from among the standard 80 options of [Ahmad et al. \(2010\)](#), based on matching L_w . They concluded that of the two parameters in the aerosol model space—fine-mode fraction (FMF) (i.e., the FMF by volume) and RH—FMF was the primary factor affecting the L_w match. Nonoptimal values were selected frequently at all three sites, leading to retrieved L_w differences, relative to in situ observation, that could exceed 40% at 412 nm, though spatial and temporal sampling differences between the satellite- and surface-based measurements in heterogeneous coastal regions could contribute significantly to this result, as could errors in the in situ L_w measurements. [McCarthy et al. \(2012\)](#) also found that FMF and the particle ANG were not related to L_w error in a simple way. However, the value and spectral dependence of SSA, another free parameter in the particle optical model, was not examined explicitly in that study, and there are limitations to the AERONET SSA retrievals as well (e.g., [Dubovik et al. 2000](#); [Dubovik and King 2000](#)). Their focus was on finding a model from among the 80 standard options that yields acceptable values of L_w ; the degree to which this generalizes to the global ocean, and to a broader range of aerosol types, was beyond the scope of their analysis.

The present study makes use of an extensive set of coincident SeaWiFS retrievals and surface-based direct-sun measurements of spectral AOD from the AERONET sun photometer federation ([Holben et al. 1998](#)). These SeaWiFS–AERONET matchups were collated by [Sayer et al. \(2012\)](#). Note, however, that the focus of [Sayer et al. \(2012\)](#) was the SeaWiFS aerosol product created as part of the NASA Making Earth System Data Records for Use in Research Environments (MEaSUREs) program, whereas the focus of the current study is the SeaWiFS Ocean Color atmospheric correction aerosol product (the two are independent datasets produced by different algorithms).

We explore statistically the patterns of differences between these SeaWiFS-derived AOD values and particle properties and AERONET "ground truth" in regimes where the aerosol contribution to TOA reflectance is dominated by a range of scattering and absorbing aerosol types. We include in our analysis the more biologically productive ocean regions (e.g., near coasts), as well as island sites near relatively clear, low-productivity ocean waters more typical of offshore marine environments. We then follow the retrieval approach adopted for the standard OBP SeaWiFS and MODIS ocean color data products to assess the implications for overestimation and underestimation of ocean surface reflectance based on

the observed AOD- and aerosol-type anomalies. In [section 2](#) we describe the coincident SeaWiFS–AERONET dataset and analyze the patterns in the SeaWiFS AOD anomaly, stratified by aerosol-type proxies. In [section 3](#) we examine the sensitivity of retrieved ocean surface reflectance to AOD and spectral slope variations, based on a nominal run of the retrieval algorithm as compared with one in which the AOD is adjusted to match that from near-coincident AERONET measurements, again stratified by aerosol-type proxies. We also compare with limited coincident surface ocean color measurements and estimate the sensitivity of retrieved chlorophyll-*a* concentration to uncertainties in the aerosol contribution to TOA reflectance, and conclusions are presented in [section 4](#).

2. SeaWiFS atmospheric correction, aerosol optical depth, and particle property patterns

[Table 1](#) lists 49 coastal and island AERONET sites used in this study, organized in order of increasing climatological AOD, with sections labeled as low-AOD maritime sites; sites typically having primarily maritime (mainly sea spray and background sulfate) particles but mixed with some dust, continental, or pollution aerosol; sites where aerosols from terrestrial sources typically make greater contributions; and sites that tend to have higher AOD and major terrestrial aerosol contributions. Note that where “AOD” appears unsubscripted, it refers to midvisible optical depth, generally assessed around 550 nm; subscripts are used to indicate other wavelengths (nm). “Continental” aerosol is typically a mix of background sulfate and soil particles, sometimes also containing biogenic or biomass burning components. The locations of these sites are shown in [Fig. 1](#). A total of 14 131 SeaWiFS–AERONET coincident events are contained in the record summarized here. These were obtained by temporally averaging cloud-screened and quality-assured level 2.0 AERONET data ([Smirnov et al. 2000](#)) within ± 30 min of a SeaWiFS overpass, and by spatially averaging SeaWiFS retrievals passing the standard set of OBPG quality checks within a 25-km radius of the AERONET site ([Sayer et al. 2012](#)). The most recent version of the SeaWiFS software was used here (SeaDAS, version 7.3, which includes the latest SeaWiFS calibration and algorithms associated with NASA standard processing version R2014.0; available at <http://oceancolor.gsfc.nasa.gov/cms/reprocessing/>); it applies final radiometric calibration to the SeaWiFS level 1A data and is also used to perform the OBPG retrievals.

The names of sites for which individual events having AOD > 0.35 occur within the dataset are indicated in [Table 1](#), illustrating that even some climatologically low-AOD sites experience high-AOD plumes at times.

Included in [Table 1](#) are the mean and standard deviation of both the AERONET and SeaWiFS AOD values in the coincident dataset at 440, 550, and 870 nm for each site, and the 440 and 870 nm (SeaWiFS – AERONET) AOD differences, computed as the numerical mean of the paired differences for each site. Also listed in the table are whether the site is coastal or island, the general geographic region, and the expected dominant aerosol types.

a. SeaWiFS AOD anomalies relative to AERONET

[Figure 2](#) provides an overview of AOD differences between the values obtained from the SeaWiFS algorithm and the corresponding AERONET values at 870 and 440 nm, stratified into bins of AERONET AOD₈₇₀. Statistically, SeaWiFS tends to overestimate AOD₈₇₀ of order 0.02 for AERONET AOD₈₇₀ < ~0.1, and it tends to underestimate AOD for larger AERONET AOD, with a maximum bin-mean underestimation, in the AOD > 0.35 bin, of about 0.28 at this wavelength ([Fig. 2a](#)). As such, SeaWiFS tends to reduce the dynamic range of the AERONET-measured AOD at 870 nm. The range of variability of the central 68% of the data, indicated by whiskers in this figure, increases systematically with AOD₈₇₀, as might be expected, in this case from about 0.05 to 0.2. [Figure 2b](#) compares the extrapolated SeaWiFS values at 440 nm with the corresponding AERONET measurements. The pattern is similar to that at 870 nm, but the AOD₄₄₀ overestimation at low AOD₈₇₀ is about 0.03 on average, and the average AOD₄₄₀ underestimation corresponding to higher AOD₈₇₀ values is about 0.5. A similar trend in AOD₄₄₀ anomalies between SeaWiFS and AERONET was observed by [Mélain et al. \(2013a,b\)](#) for an earlier version of the SeaWiFS data product and a different, but also statistically large, set of coincident observations. So the spectral slopes used to extrapolate the SeaWiFS AOD from the NIR to shorter wavelength (i.e., toward generally higher AOD values) are statistically less steep than the AERONET measurements indicate. More importantly, the variability of the bias for the SeaWiFS extrapolated values is large for the higher AOD bins, suggesting that the AOD spectral slope deviations vary considerably.

[Figure 3](#) takes a closer look at the spectral AOD anomalies. The first set of histograms ([Figs. 3a–g](#)) shows the (SeaWiFS – AERONET) AOD distributions at 870 nm, stratified by AERONET AOD₈₇₀ (each plot corresponds to one point in [Fig. 2a](#)). These histograms are monomodal and relatively compact; the SeaWiFS AOD anomalies that appear in [Fig. 2a](#) are reflected in the deviations of the histogram peak from the zero lines (dotted vertical lines) in [Figs. 3a–g](#). Not surprisingly for overocean observations, the majority of points fall in the two lowest AOD bins, where the SeaWiFS AOD

TABLE 1. Inventory of SeaWiFS–AERONET coincident cases used, showing climatological mean (standard deviation) AOD values. IMC = International Marine Center. IMS METU = Institute of Marine Sciences of Middle East Technical University. MCO = Maldives Climate Observatory.

Site	No. cases	Low-AOD maritime sites												Site type ^b	Region	Main aerosol	
		AERONET AOD 440 nm	SeaWiFS AOD 440 nm	AOD 440 nm Diff	AERONET AOD 550 nm	SeaWiFS AOD 550 nm	AERONET AOD 870 nm	SeaWiFS AOD 870 nm	AOD 870 nm Diff								
Crozet Island	52	0.058 (0.039)	0.12 (0.054)	0.066	0.056 (0.039)	0.11 (0.047)	0.051 (0.035)	0.089 (0.041)	0.038	Island	South Indian Ocean	Maritime					
Rottnest Island	181	0.064 (0.032)	0.082 (0.037)	0.018	0.059 (0.029)	0.070 (0.033)	0.044 (0.026)	0.054 (0.029)	0.0096	Coastal island	Western Australia	Maritime					
Reunion St. Denis	109	0.070 (0.031)	0.11 (0.042)	0.045	0.061 (0.025)	0.10 (0.037)	0.044 (0.019)	0.084 (0.033)	0.04	Island	Southwest Indian Ocean	Maritime					
Amsterdam Island	99	0.074 (0.038)	0.11 (0.042)	0.036	0.067 (0.037)	0.096 (0.037)	0.060 (0.037)	0.080 (0.033)	0.02	Island	South Indian Ocean	Maritime					
San Nicolas	412	0.087 (0.056)	0.13 (0.067)	0.047	0.071 (0.043)	0.11 (0.052)	0.049 (0.029)	0.071 (0.034)	0.022	Coastal island	Southern California	Maritime, pollution					
Tahiti	258	0.083 (0.035)	0.11 (0.044)	0.03	0.074 (0.029)	0.10 (0.039)	0.054 (0.026)	0.084 (0.035)	0.03	Island	South Pacific	Maritime					
Nauru	334	0.078 (0.036)	0.13 (0.056)	0.056	0.074 (0.035)	0.12 (0.048)	0.062 (0.034)	0.096 (0.040)	0.034	Island	Southwest Pacific	Maritime					
Lanai	400	0.083 (0.046)	0.13 (0.047)	0.044	0.072 (0.036)	0.11 (0.041)	0.053 (0.027)	0.088 (0.037)	0.036	Island	Hawaii	Maritime					
Trinidad Head	218	0.089 (0.057)	0.11 (0.059)	0.024	0.072 (0.046)	0.092 (0.048)	0.049 (0.035)	0.066 (0.037)	0.016	Coast	Northern California	Maritime					
Coconut Island	172	0.093 (0.055)	0.12 (0.037)	0.025	0.083 (0.044)	0.10 (0.032)	0.063 (0.033)	0.080 (0.029)	0.017	Island	Hawaii	Maritime					
Guam	59	0.094 (0.033)	0.16 (0.053)	0.062	0.090 (0.031)	0.13 (0.044)	0.071 (0.030)	0.10 (0.036)	0.031	Island	West Pacific	Maritime					
Midway Island	323	0.094 (0.048)	0.13 (0.046)	0.036	0.087 (0.042)	0.11 (0.039)	0.070 (0.037)	0.090 (0.034)	0.02	Island	Central Pacific	Maritime					
Sites having primarily maritime particles, but mixed with some dust, continental, or pollution aerosol																	
Azores	166	0.11 (0.058)	0.13 (0.055)	0.025	0.095 (0.050)	0.11 (0.043)	0.068 (0.044)	0.083 (0.030)	0.014	Island	East Atlantic	Maritime, dust					
Gustav Dalen Tower	241	0.14 (0.10)	0.15 (0.070)	0.0083	0.096 (0.078)	0.11 (0.052)	0.056 (0.050)	0.061 (0.029)	0.0042	Island	North Baltic Sea	Maritime, continental					
Tudor Hill	106	0.14 (0.075)	0.15 (0.054)	0.0097	0.12 (0.067)	0.12 (0.044)	0.085 (0.061)	0.088 (0.036)	0.0024	Island	Northwest Atlantic	Maritime, dust					
Ragged Point	117	0.097 (0.057)	0.13 (0.049)	0.037	0.092 (0.050)	0.11 (0.043)	0.078 (0.042)	0.089 (0.037)	0.011	Island	Barbados	Maritime, dust					
Bermuda	310	0.13 (0.084)	0.16 (0.058)	0.025	0.11 (0.063)	0.13 (0.046)	0.073 (0.042)	0.097 (0.033)	0.024	Island	West North Atlantic	Maritime, dust					
Cape San Juan	117	0.12 (0.078)	0.14 (0.050)	0.027	0.11 (0.069)	0.12 (0.042)	0.097 (0.062)	0.095 (0.033)	−0.0022	Island	Puerto Rico	Maritime, dust					
Graciosa	66	0.11 (0.060)	0.13 (0.064)	0.018	0.094 (0.050)	0.10 (0.051)	0.069 (0.036)	0.074 (0.039)	0.0055	Island	East Atlantic (Azores)	Maritime, dust					
La Parguera ^a	521	0.13 (0.066)	0.15 (0.055)	0.024	0.11 (0.055)	0.13 (0.047)	0.078 (0.045)	0.10 (0.040)	0.023	Coast	Puerto Rico	Maritime, dust					
Santa Cruz	281	0.14 (0.076)	0.16 (0.071)	0.017	0.12 (0.068)	0.13 (0.059)	0.088 (0.059)	0.095 (0.047)	0.01	Island	E Atlantic	Maritime, dust					
Tenerife ^a	298	0.15 (0.097)	0.16 (0.081)	0.0088	0.11 (0.074)	0.12 (0.062)	0.070 (0.047)	0.079 (0.039)	0.0095	Coast	Portugal	Continental					
Cabo da Roca	170	0.17 (0.13)	0.15 (0.084)	−0.015	0.12 (0.097)	0.11 (0.059)	0.069 (0.051)	0.057 (0.027)	−0.011	Island	Baltic	Maritime, continental					
Gotland	160	0.16 (0.084)	0.16 (0.074)	−0.0025	0.12 (0.062)	0.12 (0.056)	0.071 (0.041)	0.070 (0.037)	−0.0011	Island	Mediterranean	Maritime, continental					
Ersa	121	0.15 (0.096)	0.16 (0.075)	0.0053	0.12 (0.071)	0.13 (0.059)	0.076 (0.045)	0.088 (0.041)	0.012	Coast	Southeast Florida	Maritime, continental					
Key Biscayne	319	0.15 (0.089)	0.18 (0.070)	0.029	0.12 (0.065)	0.14 (0.055)	0.070 (0.039)	0.10 (0.039)	0.031	Island	Caribbean	Maritime, dust					
Dry Tortugas																	

TABLE 1. (Continued)

Site	No. cases	AERONET AOD 440 nm	SeaWiFS AOD 440 nm	AOD 440 nm Diff	AERONET AOD 550 nm	SeaWiFS AOD 550 nm	AERONET AOD 870 nm	SeaWiFS AOD 870 nm	AOD 870 nm Diff	Site type ^b	Region	Main aerosol
Sites where Aerosol from terrestrial sources typically make greater contribution												
Lampedusa ^a	443	0.17 (0.10)	0.17 (0.076)	-0.0041	0.14 (0.080)	0.13 (0.059)	0.089 (0.060)	0.084 (0.040)	-0.0049	Island	Mediterranean	Dust, pollution
IMC	410	0.19 (0.099)	0.17 (0.072)	-0.019	0.14 (0.074)	0.13 (0.052)	0.082 (0.050)	0.077 (0.031)	-0.0054	Island	Mediterranean	Dust, pollution
Oristano ^a												
Dahkla ^a	98	0.13 (0.062)	0.13 (0.057)	-0.0089	0.12 (0.059)	0.10 (0.048)	0.086 (0.052)	0.078 (0.038)	-0.0075	Coast	West Sahara	Dust
Helgoland	173	0.19 (0.10)	0.20 (0.088)	0.012	0.14 (0.077)	0.15 (0.064)	0.083 (0.043)	0.084 (0.038)	0.0018	Island	North Sea	Maritime
COVE ^a	749	0.24 (0.23)	0.21 (0.14)	-0.034	0.17 (0.17)	0.15 (0.10)	0.084 (0.079)	0.084 (0.047)	-0.00053	Coast	Chesapeake	Pollution
Sevastopol	382	0.22 (0.11)	0.19 (0.084)	-0.026	0.16 (0.081)	0.14 (0.062)	0.081 (0.045)	0.078 (0.036)	-0.0033	Coast	Black Sea	Maritime, pollution
Ascension Island	314	0.18 (0.10)	0.18 (0.071)	0.0052	0.15 (0.082)	0.16 (0.058)	0.11 (0.061)	0.12 (0.044)	0.0089	Island	South Atlantic	Maritime, smoke
MVCO ^a	283	0.17 (0.19)	0.14 (0.10)	-0.025	0.12 (0.14)	0.11 (0.074)	0.068 (0.086)	0.055 (0.035)	-0.012	Coastal island	Martha's Vineyard	Maritime, continental
Forth Crete ^a	599	0.22 (0.099)	0.18 (0.066)	-0.031	0.16 (0.077)	0.14 (0.050)	0.098 (0.055)	0.085 (0.034)	-0.013	Island	Mediterranean	Dust, pollution
Kaashidhoo	156	0.21 (0.11)	0.22 (0.072)	0.012	0.16 (0.086)	0.18 (0.058)	0.10 (0.051)	0.13 (0.043)	0.028	Island	Indian Ocean	Maritime, pollution
Messina ^a	301	0.21 (0.12)	0.16 (0.067)	-0.049	0.16 (0.096)	0.12 (0.050)	0.092 (0.069)	0.074 (0.032)	-0.019	Coast	Sicily	Maritime, dust
Villefranche ^a	517	0.23 (0.15)	0.17 (0.092)	-0.055	0.16 (0.11)	0.13 (0.068)	0.084 (0.059)	0.075 (0.039)	-0.0093	Coast	South France	Maritime, continental
Capo Verde ^a	373	0.17 (0.085)	0.18 (0.074)	0.014	0.15 (0.077)	0.15 (0.062)	0.13 (0.067)	0.12 (0.049)	373	Island	East Atlantic	Maritime, dust
Sites tending to have higher AOD and major terrestrial aerosol contributions												
Inhaca ^a	72	0.23 (0.14)	0.20 (0.093)	-0.023	0.17 (0.10)	0.16 (0.065)	0.090 (0.046)	0.091 (0.033)	0.0011	Coastal island	Mozambique	Continental, smoke
MALE	66	0.24 (0.13)	0.23 (0.085)	-0.009	0.19 (0.096)	0.19 (0.066)	0.12 (0.054)	0.14 (0.047)	0.022	Island	North Indian Ocean	Maritime, pollution
Shirahama ^a	504	0.24 (0.15)	0.22 (0.083)	-0.025	0.18 (0.11)	0.17 (0.061)	0.10 (0.061)	0.099 (0.035)	-0.0033	Coast	East Japan	Maritime, pollution
Venise ^a	1453	0.28 (0.22)	0.20 (0.10)	-0.08	0.21 (0.17)	0.15 (0.073)	0.11 (0.097)	0.082 (0.041)	-0.024	Coast	Italy	Maritime, continental
IMS METU Erdemli ^a	829	0.26 (0.15)	0.19 (0.079)	-0.069	0.20 (0.11)	0.15 (0.062)	0.11 (0.064)	0.087 (0.041)	-0.023	Coast	Southwest Turkey	Maritime, continental
Arica ^a	472	0.29 (0.13)	0.23 (0.077)	-0.059	0.23 (0.099)	0.18 (0.058)	0.13 (0.052)	0.10 (0.035)	-0.031	Coast	Chile	Pollution
MCO Hani-maadho	92	0.29 (0.12)	0.26 (0.074)	-0.038	0.23 (0.093)	0.20 (0.059)	0.13 (0.058)	0.13 (0.044)	-0.0031	Island	North Indian Ocean	Maritime, pollution
Island												
Dakar ^a	131	0.21 (0.088)	0.19 (0.089)	-0.016	0.18 (0.079)	0.16 (0.073)	0.14 (0.068)	0.11 (0.057)	-0.034	Coast	Senegal	Dust
Hong Kong	4	0.21 (0.15)	0.19 (0.065)	-0.025	0.17 (0.11)	0.14 (0.048)	0.092 (0.054)	0.084 (0.025)	-0.008	Coast	China	Pollution, dust
Hok Tsui												
Gosan-SNU	100	0.32 (0.17)	0.28 (0.11)	-0.037	0.25 (0.13)	0.21 (0.080)	0.15 (0.081)	0.12 (0.043)	-0.034	Coastal island	South Korea	Pollution, dust

^a Sites having specific events with midvisible AOD > 0.35 identified in the current dataset.^b These classifications are qualitative; "coast" and "coastal island" are more likely to be influenced by runoff or pollution than remote islands, but conditions at individual sites vary with season and other factors.

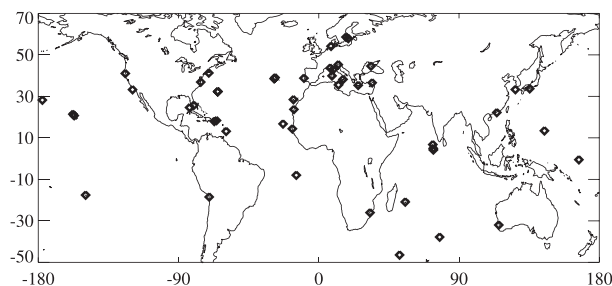


FIG. 1. Locations of AERONET sites used in this study.

anomaly tends to be positive (Figs. 3a and 3b contain 9809 points, from a total of 14 131). The second set of histograms (Figs. 3h–n) show the corresponding (SeaWiFS – AERONET) AOD distributions at 440 nm. The widths and AOD₄₄₀ underestimation grow with AOD, and the distributions become roughly bimodal for AOD₈₇₀ > ~0.2 (Figs. 3l–n), though the data volume in the higher AOD bins is limited. We explore the implications of the AOD patterns next, by stratifying the data using proxies that help distinguish between aerosols having different microphysical properties.

b. The relationship between aerosol type and AOD anomalies

Figure 4 presents the distribution of (SeaWiFS – AERONET) AOD₄₄₀ anomalies as a function of AERONET AOD₄₄₀, stratified by proxies for aerosol type. For Figs. 4a and 4b, the entire SeaWiFS–AERONET coincident dataset is included, stratified and color-coded by AERONET-derived ANG. ANG is defined as the negative slope of the AOD versus wavelength regression line, in logarithmic coordinates, and is used here as a rough proxy for aerosol type. It is assessed for wavelengths between 440 and 870 nm for AERONET, and between 443 and 865 nm for SeaWiFS. In general,

ANG decreases with increasing effective particle size, though the situation is complicated when two or more aerosol modes are present (e.g., Schuster et al. 2006). Typical smoke and pollution particles fall primarily in the small- to medium-size range, producing ANG values generally greater than unity, whereas dust and sea salt populations are typically dominated by larger particles and tend to have ANG below about 0.8 (e.g., Eck et al. 1999; Dubovik et al. 2002).

As in Fig. 2, the plots in Fig. 4 show SeaWiFS AOD₄₄₀ is overestimated at low AERONET AOD and is underestimated at higher AERONET AOD, resulting in SeaWiFS AOD having a lower dynamic range compared to AERONET. However, there are also systematic differences correlated with aerosol type, even based on the available, relatively crude proxies. The fine-mode-dominated particles (ANG > 1; black, red, orange, and yellow points) plotted in Fig. 4a are clustered closer to the zero line than the coarse-mode-dominated particles, which is easiest to see by comparing Fig. 4c (fine mode) with Figs. 4d and 4e (dust and maritime strata), or from looking at Tables 2 and 3. The fine-mode point cloud also has a shallower slope and tends to be weighted below the zero line (AOD underestimation) for AOD₄₄₀ larger than about 0.3. These anomaly patterns are better characterized numerically: for AOD₄₄₀ < 0.25, the mean AOD anomaly for points having ANG > 1 is 0.009, whereas for points having ANG < 0.8 it is higher (0.035); for AERONET AOD between 0.25 and 0.4, the corresponding values are –0.069 and –0.0464, respectively.

As a second proxy for aerosol type, several sites were selected that tend to be dominated by either fine-mode (mainly pollution and smoke), dust, or maritime particles (Table 1), and the (SeaWiFS – AERONET)

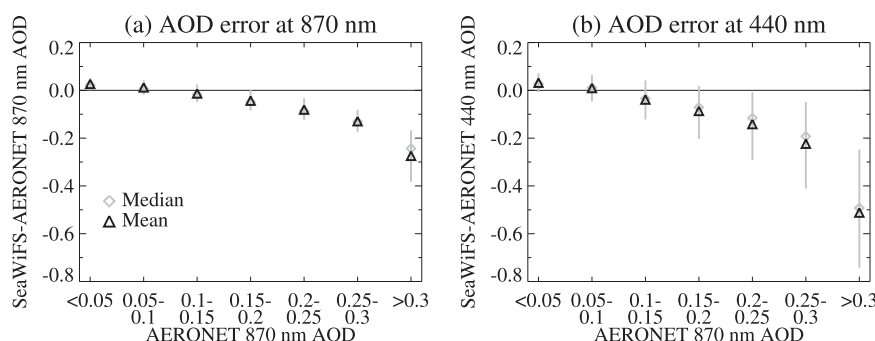


FIG. 2. Mean and median differences between the SeaWiFS algorithm spectral AOD and the corresponding AERONET measurements for the 14 131 coincidences summarized in Table 1, stratified by AERONET AOD₈₇₀. (a) (SeaWiFS – AERONET) AOD at 870 nm, and (b) (SeaWiFS – AERONET) AOD at 440 nm. Whiskers indicate the central 68% of data in each bin.

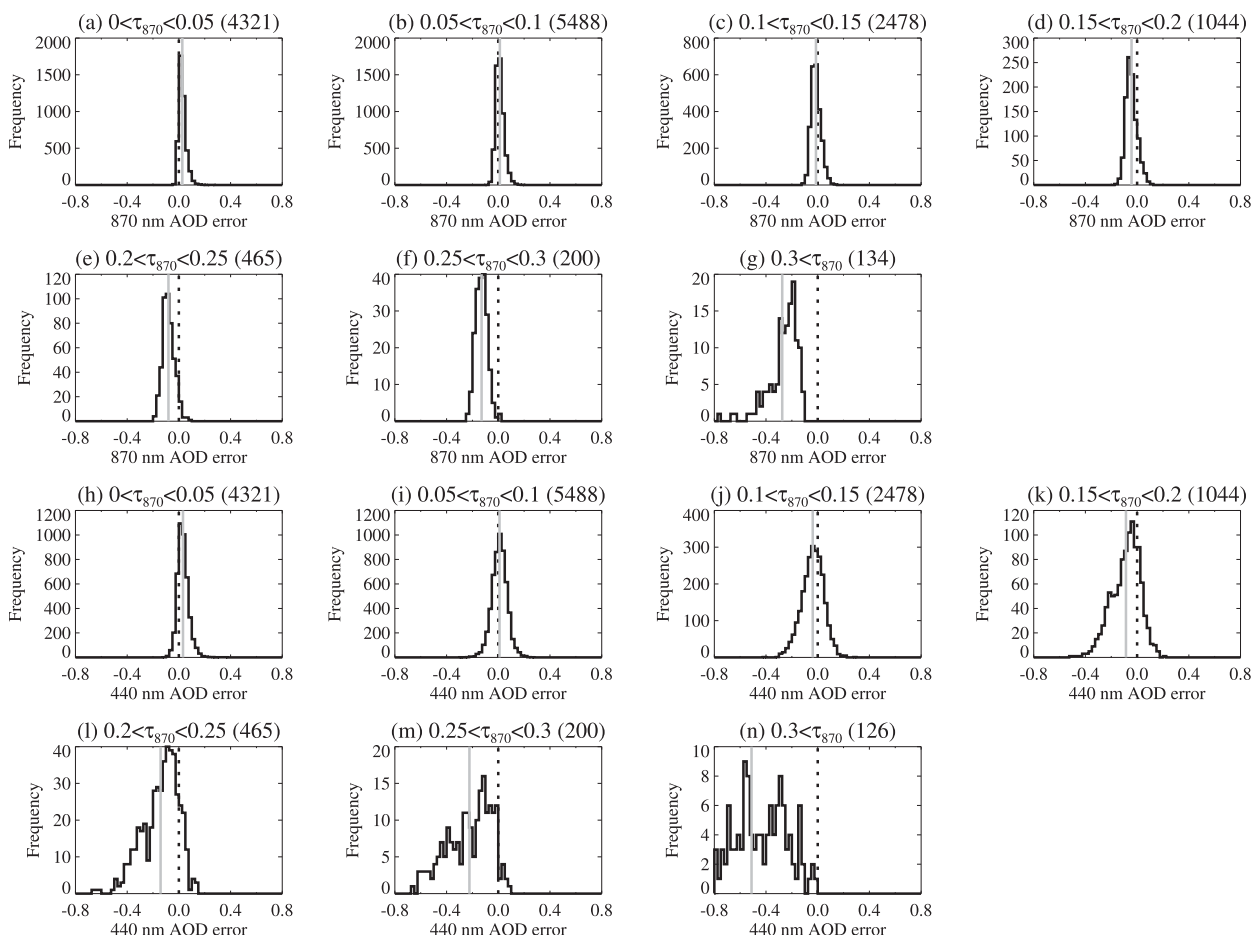


FIG. 3. Histograms showing the distribution of (SeaWiFS – AERONET) AOD anomalies for the coincidences summarized in Table 1, stratified by AERONET AOD₈₇₀. (a)–(g) AOD anomalies at 870 nm; (h)–(n) AOD anomalies at 440 nm. Dotted black lines mark zero, solid gray lines indicate the mean value in each plot, and the counts are given in parentheses in the individual plot titles.

AOD₄₄₀ anomalies for these three groups of sites are plotted separately in Figs. 4c–e, respectively. Color is used to indicate the density of points in these three plots. To reduce the number of individual events where other aerosol types might have dominated at a site commonly influenced by the designated type, the fine-mode data were filtered to exclude cases for which $ANG < 1$, and the data collected at predominantly dusty sites were filtered to exclude points for which $ANG > 0.8$. This removes 22% of the fine-mode-site cases and 39% of the dust-site cases. The diagonal black lines in Fig. 4 indicate the exclusion zone, because AOD is positive definite, so (SeaWiFS – AERONET) AOD cannot be smaller than (–AERONET) AOD. These lines also provide a convenient marker showing the degree to which the negative SeaWiFS AOD₄₄₀ anomaly increases with increasing AERONET AOD₄₄₀.

As might be expected, the remote maritime plot (Fig. 4e) shows hardly any cases with AOD₄₄₀ exceeding 0.2.

Compared to the fine-mode-dominated sites (Fig. 4c), the dust-dominated sites (Fig. 4d) produce larger positive deviations at low AOD on average, and possibly a steeper negative slope at higher AOD. Note that AOD tends to increase toward shorter wavelengths, and for larger particles, we expect the spectral slope of AOD to be reduced (smaller ANG). So, other things being equal, more coarse-mode than fine-mode AOD at 870 nm would be required to produce a given AOD at 440 nm; as such, cloud screening applied at 870 nm might contribute to the relative paucity of coarse-mode data points having AOD₄₄₀ > 0.4.

Tables 2 and 3 provide a more quantitative description of these patterns, reporting regression line fits to the AOD anomaly data in each plot of Fig. 4, separately for AERONET AOD₄₄₀ < 0.25 (Table 2) and for 0.25 < AERONET AOD₄₄₀ < 0.40 (Table 3), two approximate regimes based on Fig. 4. Because of the small number of high-AOD maritime cases, we truncate the regression analysis above AOD₄₄₀ of 0.25. For AOD₄₄₀ < 0.25, the

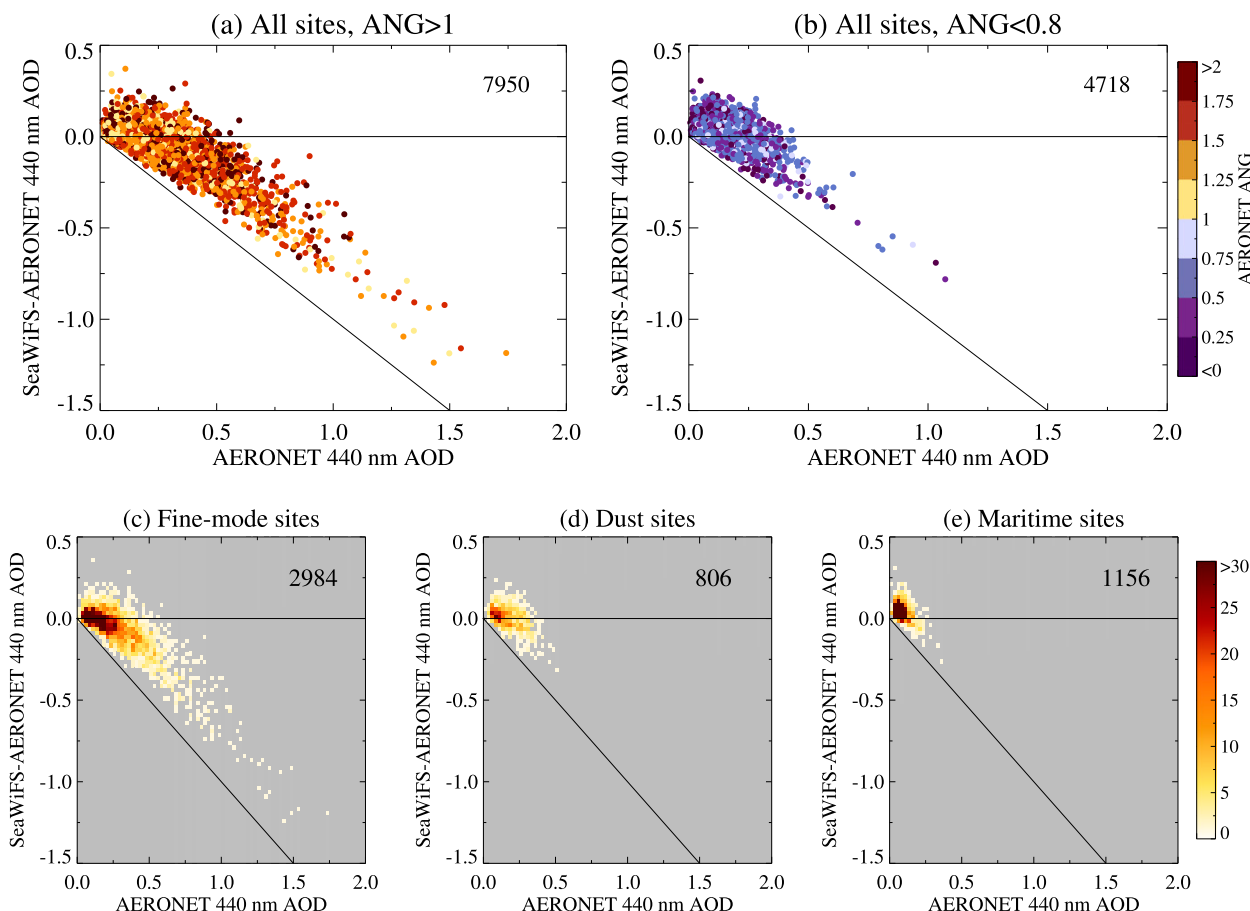


FIG. 4. Scatter and density plots showing $(\text{SeaWiFS} - \text{AERONET}) \text{AOD}_{440}$ anomaly vs $\text{AERONET} \text{AOD}_{440}$, stratified by proxies for aerosol type: all coincidences summarized in Table 1, color-coded by the AERONET ANG, and stratified so (a) cases dominated by small-medium particles ($\text{ANG} > 1$) and (b) cases dominated by larger particles ($\text{ANG} < 0.8$), (c) scatter-density plot of AOD_{440} anomaly for nine representative fine-mode-dominated (mainly pollution or smoke) sites (Arica, Ascension Island, COVE, Gosan-Seoul National University (SNU), Hong Kong Hok Tsui, Inhaca, Kaashidhoo, Venice, Villefranche), (d) five representative dust-dominated sites (Capo Verde, Dakar, Dahkla, Lampedusa, Santa Cruz Tenerife), and (e) four representative maritime-dominated sites (Amsterdam Island, Lanai, Midway Island, Nauru). Data for fine-mode sites [(c)] have been filtered to include only $\text{ANG} > 1.0$ cases, and those for the dust-dominated sites [(d)] include only cases where $\text{ANG} < 0.8$; the unfiltered patterns (not shown) are very similar, but for fine mode, they exhibit more scatter. The color bars for (c)–(e) indicate the binned data counts, and the diagonal black lines mark the exclusion zone, because $(\text{SeaWiFS} - \text{AERONET}) \text{AOD}$ cannot be smaller than $(-\text{AERONET} \text{AOD})$. The number of points included is given in the upper right of each plot.

fine-mode subset has a smaller positive offset than the dust and maritime sites, as can be seen qualitatively from the plots. The correlation coefficients (R values in Table 2) are all very low in this regime, as the data tend to cluster around the offsets (regression line c coefficients in Table 2), which are 0.046 for fine mode and 0.056 for dust. The correlations at higher AOD (Table 3) are often greater, though the maritime category is too poorly sampled in this regime to provide meaningful statistics and so is omitted. In addition, because of the generally low background maritime AOD, it is plausible that high-AOD cases at the “maritime” sites represent cases of transported nonmarine aerosol rather than elevated maritime AOD.

Figure 5 presents the relationships between ANG and the AOD anomaly, with the ANG anomaly represented as the deviation from the 1:1 lines drawn in each panel, stratified by aerosol-type proxy as in Fig. 4. As with AOD, the dynamic range of ANG is reduced in SeaWiFS compared to AERONET (i.e., ANG is overestimated at lower ANG and underestimated at higher ANG). But there are distinct differences among the aerosol-type proxies. For the coarse-mode-dominated dust stratum (Fig. 5c), ANG is systematically overestimated for most of the ANG range, independent of the AOD anomaly, whereas for fine-mode-dominated aerosol, the ANG anomaly distribution is centered more

TABLE 2. Linear regression fits to the data in each panel of Fig. 4, for AERONET $\text{AOD}_{440} \leq 0.25$. Here x is the AERONET AOD_{440} and y is the (SeaWiFS – AERONET) AOD_{440} anomaly.

AOD_{440}	$y = a(\pm b)x + c(\pm d)$				R
	a	b	c	d	
$\alpha > 1.0$	−0.342	0.011	0.055	0.002	0.39
$\alpha < 0.8$	−0.317	0.014	0.069	0.002	0.34
Fine mode	−0.300	0.021	0.046	0.003	0.33
Dust	−0.24	0.038	0.056	0.006	0.24
Maritime	−0.438	0.031	0.082	0.003	0.38

closely to the zero line or ANG is even slightly underestimated on average (Fig. 5b), though still with a fairly large spread. This accounts for the systematic AOD_{440} overestimation for the dust proxy in Fig. 4; as AOD increases toward shorter wavelengths, the steeper slope represented by ANG overestimation tends to produce an AOD_{440} overestimation for these particles. Also note that a majority of the points having large negative AOD_{440} anomaly are fine mode, and that there are subsets of cases with a large negative AOD anomaly for which the SeaWiFS ANG tends to be underestimated, for the fine mode and dust strata (Figs. 5b and 5c, some purple points). This could reflect the flatter single-scattering phase functions in the side-scattering directions viewed by satellites, and associated with particles that are small relative to the wavelength of light and also for nonspherical dust particles (e.g., Kahn et al. 1998; see also discussion in section 2c below). As such, the spectral dependence of AOD estimated by the SeaWiFS algorithm, as well as the AOD_{440} anomaly, is particle-type dependent.

Each of the proxies used in Figs. 4 and 5 has limitations. For example, the smoke and dust contributions to AOD at characteristic sites vary considerably with season, but having stratified the data in several ways, we can still draw the conclusion that aerosol type appears to play a role in the observed SeaWiFS AOD anomalies. For AOD_{440} less than about 0.2, the AOD_{440} anomalies tend to be positive for all aerosol types and are statistically more positive for dust than for characteristically fine-mode particles. Likely pollution and smoke cases, generally having the largest absorption at visible wavelengths and identified based on proxy indicators, also produce smaller AOD anomalies (shallower negative slope) in the higher-AOD regime. However, the fine-mode cases in this dataset extend to much higher AOD values than for the other aerosol types, and they dominate the negative anomaly cases overall. Note that there is an additional subtlety: to obtain accurate L_w values, both aerosol extinction and aerosol scattering must be represented adequately. We explore this in the next section.

TABLE 3. Linear regression fits to the data in each panel of Fig. 4, for $0.25 < \text{AERONET } \text{AOD}_{440} < 0.40$. Data for the maritime subset are omitted, as maritime AOD of this magnitude is statistically less common. Here x is the AERONET AOD_{440} , and y is the (SeaWiFS – AERONET) AOD_{440} anomaly.

AOD_{440}	$y = a(\pm b)x + c(\pm d)$				R
	a	b	c	d	
$\alpha > 1.0$	−0.591	0.040	0.115	0.013	0.34
$\alpha < 0.8$	−0.824	0.097	0.203	0.030	0.40
Fine mode	−0.606	0.066	0.124	0.021	0.33
Dust	−0.685	0.158	0.166	0.048	0.32
Maritime	—	—	—	—	—

c. Aerosol type, single-scattering albedo, and AOD anomaly

AERONET direct-sun observations determine the extinction AOD, which is the sum of scattering and absorption, by calculating the transmittance of the direct solar beam. In contrast, most satellite instruments measure backscattered solar radiation and must assume or deduce the absorption component of the AOD. Depending on aerosol type, the absorption and scattering contributions can be overestimated or underestimated when values in the shortwave ocean color retrieval spectral region are deduced from measurements at longer wavelengths or are otherwise determined.

Smoke and pollution aerosols tend to absorb across the visible spectrum, but although absorption itself increases toward shorter wavelengths, the fraction of light absorbed versus scattered tends to decrease (which produces higher SSA toward the blue, though still < 1) (e.g., Russell et al. 2010). Saharan desert dust also absorbs in the infrared, though generally much less than smoke (e.g., Sokolik and Toon 1999). However, unlike smoke or pollution particles, red Saharan dust typically absorbs much more strongly toward shorter visible wavelengths. As airborne particles age, especially smoke and pollution, they tend to oxidize and become increasingly hygroscopic, both of which move the SSA toward unity. The challenge here is that SSA is much more difficult to constrain than AOD with remote sensing observations. Even with AERONET, for example, $\text{AOD}_{440} > 0.4$ and solar zenith angle $> 50^\circ$ are required to obtain good-quality SSA values, with an approximate uncertainty of 0.03 (Dubovik et al. 2000). As such, favorable remote sensing SSA retrieval conditions are rarely met over most of the ocean; however, over remote ocean, SSA tends toward unity for transported or locally generated aerosol. So over ocean, absorbing particles are more likely to be found nearer to aerosol sources, such as over some coastal waters, which are often also regions of greater

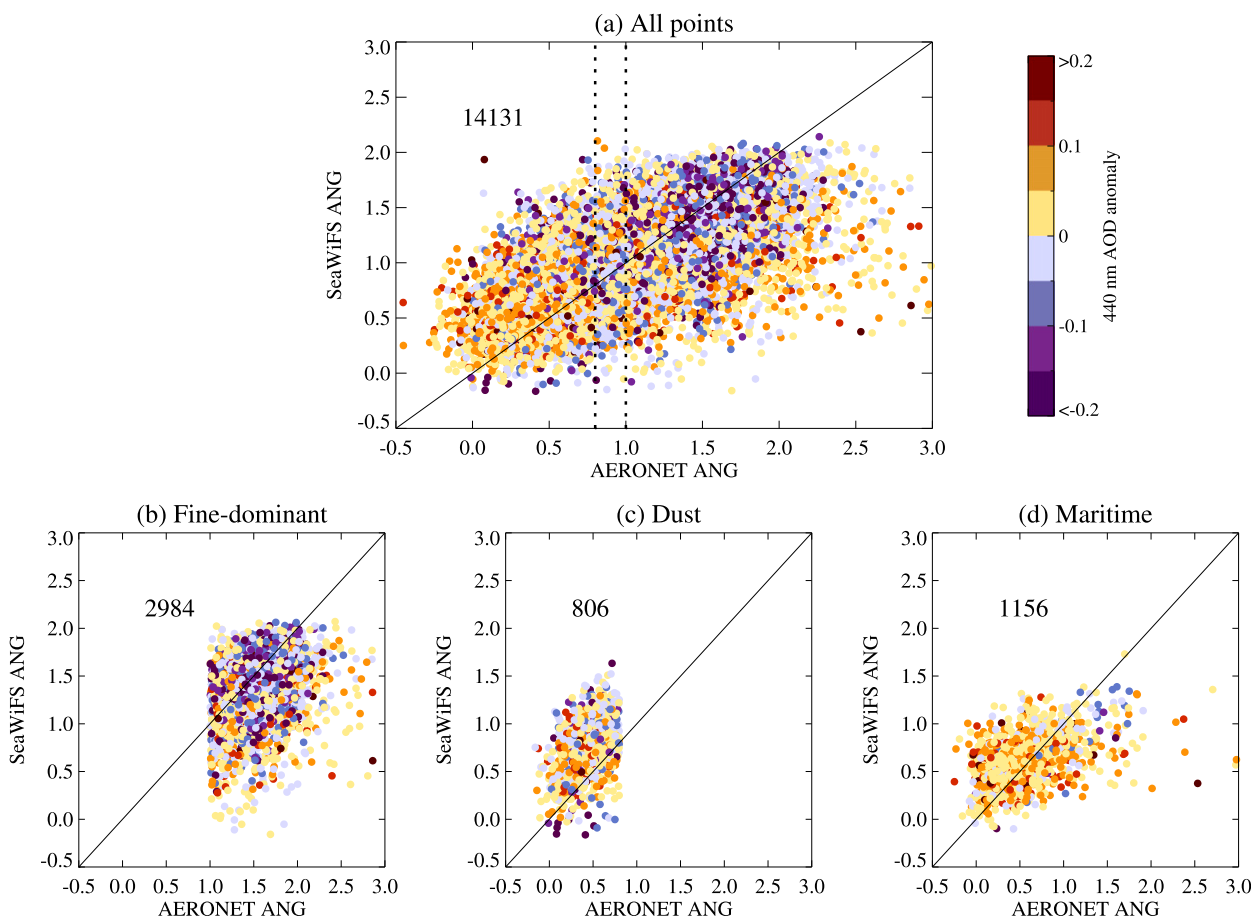


FIG. 5. Scatterplots showing SeaWiFS ANG vs AERONET ANG, colored by the AOD₄₄₀ anomaly: (a) all points and (b)–(d) stratified by the same aerosol-type proxies applied in Figs. 4(c)–(e), respectively. The number of points included is given in the upper left of each plot.

biological productivity and therefore of considerable interest for ocean color.

To determine how the combined derivation of AOD₄₄₀ and aerosol scattering properties affects atmospheric correction in practice, the particle-type selections made in the standard OBPG processing need to be examined in more detail. The effect should be most pronounced in regions of relatively high AOD, so we concentrate on such cases for the purpose of identifying the phenomenon and quantifying it, to the extent possible. The SSA remote sensing retrieval itself requires relatively high AOD as well. However, in addition to AOD and single-scattering phase function effects, uncompensated SSA is also likely to skew results at lower AOD.

Figure 6 illustrates the AOD, SSA, and particle scattering asymmetry (ASY) values for a few individual cases where coincident AERONET and SeaWiFS data are available. In all these cases, the AOD is high enough to meet the AERONET requirement for good-quality

SSA and ASY retrievals (AOD₄₄₀ > 0.4); the corresponding baseline SeaWiFS AOD₄₄₀ values are systematically low, as expected from Fig. 2 above. Also shown are AOD values from the SeaWiFS retrieval when the SeaWiFS spectral AOD was constrained to align as closely as possible with the AERONET value (gray lines) (Franz et al. 2001), though other particle microphysical properties are only partly constrained by AERONET in this process (see section 3 below). SSA is generally overestimated in the SeaWiFS retrievals (i.e., reporting weaker absorption than AERONET), though by varying amounts.

The asymmetry parameter ASY depends upon the adopted particle size and to some extent on SSA. The degree to which ASY can be constrained by the retrieval algorithm depends on observing geometry. It is included in Fig. 6 because it is a first-order constraint on the single-scattering phase function. The single-scattering phase function, assessed at the scattering angle of the satellite observation, is a part of any self-consistent

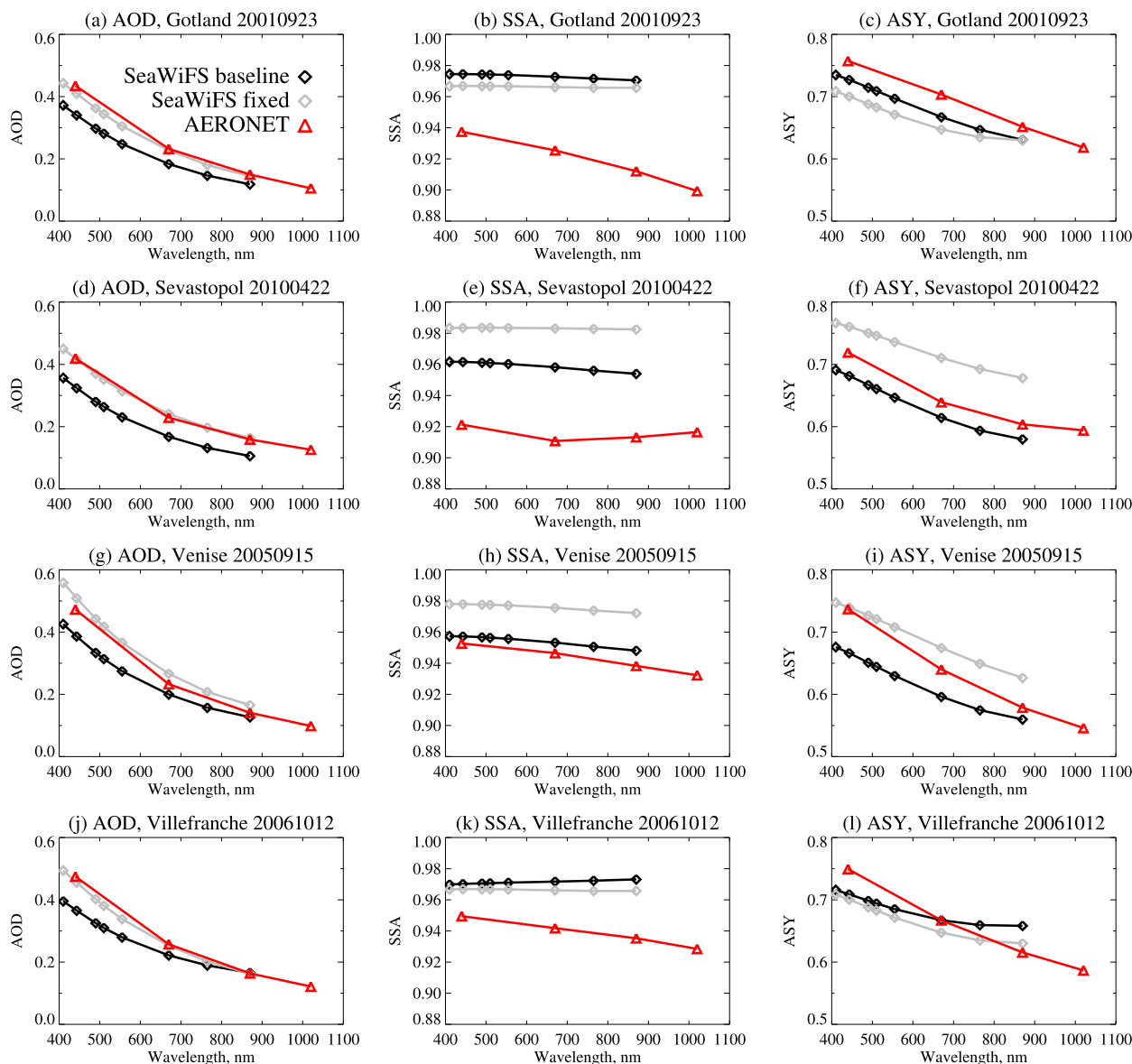


FIG. 6. A sampling of individual cases where AERONET aerosol type and SeaWiFS retrieval matchups occur (a)–(c) Gotland, in the Baltic Sea; (d)–(f) Sevastopol, in the Black Sea; (g)–(i) Venice, Italy; and (j)–(l) Villefranche, on the French Riviera; and the spectral AOD retrieval (left column), the SSA (middle column), and the ASY parameter (right column). AERONET values are presented in red, the corresponding aerosol attribute from the baseline SeaWiFS processing is given in black, and the SeaWiFS processing for which the AOD was constrained to match the AERONET values is shown in gray.

radiance-based aerosol remote sensing retrieval. As such, errors in the adopted value of the asymmetry parameter contribute to the overall uncertainty in the calculation of aerosol contributions to the top-of-the-atmosphere radiance. However, like the AERONET SSA data, AERONET asymmetry parameter data are very limited compared to the direct-sun AOD values, and entail significant uncertainties compared to the AOD values (Dubovik et al. 2000; Kahn and Gaitley 2015). We note from Fig. 6 that for the cases shown, the

variations in SeaWiFS ASY values are not systematic compared to AERONET, though the signs, but not the magnitudes, of the spectral slopes are consistent. We focus on SSA in the subsequent discussion, to the extent possible, with the understanding that uncertainty in the single-scattering phase function represents an additional uncertainty factor.

Figure 7 takes a more robust statistical approach, aggregating by month all available AERONET and SeaWiFS SSA cases separately, for all events meeting

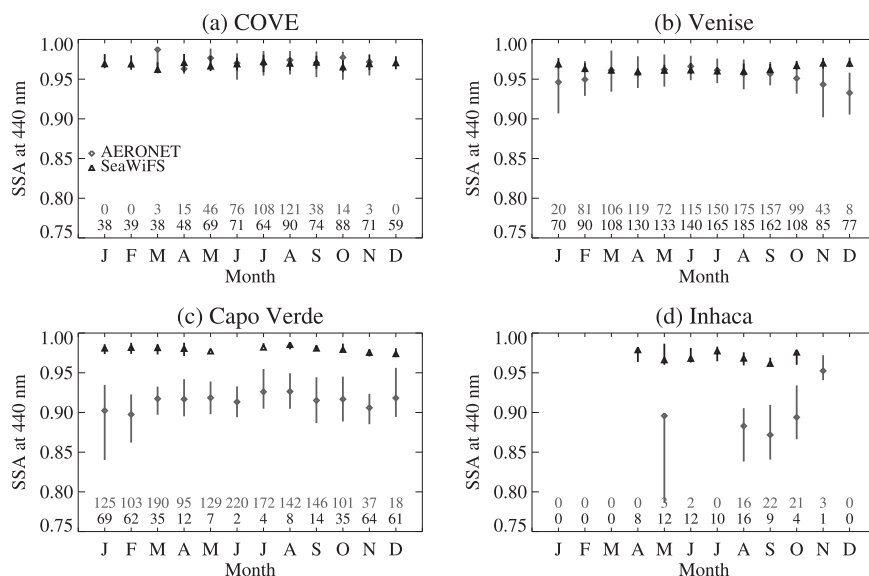


FIG. 7. Monthly aggregated SSA values derived from AERONET observations (gray) and as obtained from SeaWiFS retrievals (black) at four sites (a) COVE, a moderately polluted site at the outlet of Chesapeake Bay, Virginia; (b) Venice, on the northeast coast of Italy; (c) Capo Verde, an island site downwind of the Sahara Desert; (d) Inhaca, on the east coast of Mozambique, downwind of heavy seasonal burning in southern Africa. All available data meeting the respective high-quality retrieval criteria are included in these summary median values (symbols) and the central 68% of the data (whiskers). The number of counts from each dataset is given along the bottom of each plot; the data are not plotted if there are fewer than four points in the aggregated month.

the respective high-quality retrieval criteria. Again, the SSA in the SeaWiFS processing is systematically overestimated. It attains values between about 0.96 and 0.98 even as the AERONET SSA varies between similar values and ones below 0.90. This is not surprising, as the lowest SSA_{440} within the suite of models in the current SeaWiFS algorithm is 0.95 (Ahmad et al. 2010).

However, it is important to note that AERONET SSA has a sampling bias toward high-AOD conditions, whereas SeaWiFS has a sampling bias toward low-AOD conditions. As the SSA of unpolluted maritime aerosol is typically close to unity, it is expected on sampling grounds that SeaWiFS SSA could be higher than AERONET SSA when a climatology is constructed in this way. Still, these climatologies are broadly consistent with the collocated data in Fig. 6, in that SeaWiFS tends to assign less-absorbing aerosol models than those indicated by coincident AERONET inversions when more absorbing aerosols are present.

In summary, the AOD used for SeaWiFS atmospheric correction is systematically overestimated at low AOD and underestimated at higher AOD (Fig. 2) but to degrees that vary with proxies for aerosol type, as shown in Fig. 4 and quantified in Tables 2 and 3. AOD spectral slope tends to be overestimated for coarse-mode particles

(Fig. 5), and SSA seems to be overestimated wherever the value is likely to be lower than about 0.96 (Fig. 7), though validation data are very limited for the SSA assessment. We now examine how the aerosol anomalies might affect the retrieved L_w and chlorophyll-*a* concentration values.

3. The impact of AOD anomalies on SeaWiFS-derived water-leaving reflectance and chlorophyll-*a* concentration

The AOD anomalies summarized in section 2, and the apparent relationship between aerosol type and the sign and magnitude of these anomalies, suggest that not only the absolute magnitude of derived ocean surface parameters, but also the relative spatial patterns, could be influenced by errors in the aerosol amount and type used for atmospheric correction. In this section we assess the sensitivity of derived water-leaving reflectance over- and underestimation, and consider possible impacts on SeaWiFS-derived chlorophyll-*a* concentration, implied by the range of observed AOD and associated aerosol-type anomalies in the SeaWiFS–AERONET dataset.

To assess R_{rs} sensitivity, we performed two runs of the SeaDAS code for the SeaWiFS–AERONET coincident events summarized in Table 1: a “baseline” run, in

which AOD_{440} was determined using the SeaDAS, version 7.3, operational method, and a “fixed AOD” run. For the fixed-AOD run, AERONET AOD values were incorporated into the SeaWiFS retrieval process based on the approach of Franz et al. (2001). The SeaWiFS standard radiative transfer model (Franz et al. 2001), constrained with AERONET-measured spectral AOD interpolated to the SeaWiFS wavelengths, was used to calculate the aerosol scattering contribution to the TOA radiances. Other aerosol microphysical properties (e.g., SSA), which are needed to compute aerosol path radiance from AERONET-measured AOD, were obtained from the suite of 80 aerosol models, by finding the nearest model that matches both the Ångström exponent inferred from the AERONET AODs and the RH at the time of observation. The ocean color retrieval was then performed, by subtracting the AERONET-based aerosol path radiances from the TOA radiances in each SeaWiFS visible band. All other contributions and corrections required to derive R_{rs} from TOA radiance (e.g., Rayleigh scattering) were computed consistently with the baseline atmospheric correction procedure.

The residual spectral AOD error from this fitting process, relative to the actual AERONET value, was small: the median biases (fixed-AERONET AOD) were negligible (0.0007 at 440 nm, 0.0008 at 870 nm) and the standard deviations (0.012 at 440 nm, 0.004 at 870 nm) were comparable to or smaller than the AERONET AOD uncertainty. Note that SSA and other aerosol microphysical properties were not constrained explicitly by AERONET observations due to a lack of AERONET values in most cases. As such, the fixed-AOD run might, but does not necessarily, yield truer R_{rs} values. However, the comparison shows how the algorithm responds when a key factor in the atmospheric correction is better constrained.

The fixed-AOD approach guarantees the AOD_{440} value applied is of AERONET quality but precludes some other corrections in the algorithm, such as compensation for residual stray light and cloud edge reflectance that would otherwise be taken into account and removed as residual aerosol reflectance (Franz et al. 2007). A consequence of the fixed-AOD algorithm procedure is that some of the standard quality control tests within the dataset cannot be applied, which results in a decrease of the number of pixels passing quality tests in the fixed-AOD run, such that 13 295 of the original 14 131 matchups remain valid. Only these 13 295 matchups are discussed hereafter and are included in subsequent figures.

a. SeaWiFS-derived water-leaving reflectance anomaly patterns

The primary ocean color data product is L_w or R_{rs} , and others, such as chlorophyll-*a*, are derived from these

quantities. Figure 8 compares the SeaWiFS-derived R_{rs} values when the AOD used for atmospheric correction is the baseline SeaDAS value versus when the AERONET “fixed” value is used, as a function of SeaWiFS – AERONET AOD_{440} difference. The R_{rs} differences are positive when the SeaWiFS baseline AOD is underestimated (i.e., when SeaWiFS assigns less of the TOA reflectance to the atmosphere than indicated by AERONET), as might be expected, and conversely R_{rs} differences are negative when the SeaWiFS baseline AOD is overestimated. The effects are greatest for the extrapolated R_{rs} values at 443 nm and gradually reduce toward the longer wavelengths, consistent with patterns shown in Figs. 2 and 3. In addition, the shapes of the distributions are similar across the wavelength range, indicating a spectral correlation in the R_{rs} differences introduced by the AOD anomaly.

Differences in the slopes for the aerosol-type strata in row 3 of Fig. 8 are subtle. For the larger dust and maritime particle types, the AOD anomaly tends to be positive and the baseline–fixed R_{rs} differences are mostly negative, especially at 443 nm, whereas for fine-mode-dominated conditions, the point cloud tends to be centered around the zero mark of both axes. These R_{rs} patterns are consistent with the AOD anomaly patterns shown in Fig. 4, illustrating that the aerosol-type-dependent AOD patterns are reflected in the derived R_{rs} values used to determine ocean color variables.

The effect of systematic SSA overestimation (Fig. 7), resulting in a greater assumed aerosol scattering contribution to the TOA reflectance, is most likely to appear at higher AOD, when aerosol microphysical properties matter most to the TOA signal. The systematic AOD underestimation at higher AOD would mitigate to some degree the SSA overestimation for the atmospheric correction, that is, when the TOA reflectance is interpreted in terms of atmospheric and surface-scattering signals, the underestimated aerosol amount is partly offset by having it scatter more efficiently. Quantitatively, these effects should complicate interpretation of the derived surface signal in other ways (e.g., the more absorbing aerosol would absorb more sunlight and block more of the surface signal than is considered in the retrieval). However, such effects are too subtle to show up in the validation data available for Fig. 8, although given the analysis of AOD and SSA in section 2, they are likely to impose systematic, quantitative anomalies on ocean color products that would best be tested when a richer set of validation data becomes available.

b. Comparisons with in situ ocean surface observations

To more fully assess the impact of atmospheric correction anomalies on derived ocean color quantities, and

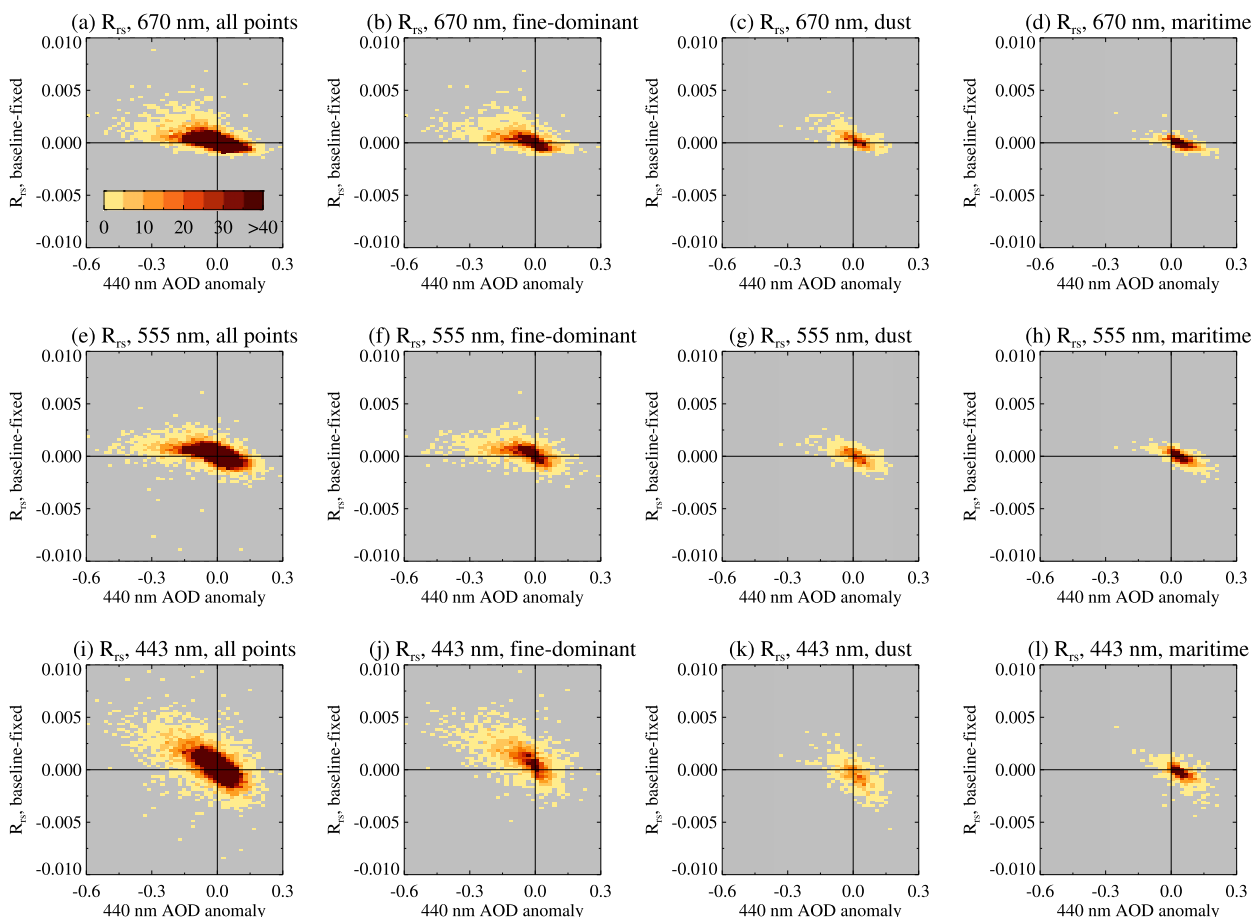


FIG. 8. SeaWiFS ocean surface spectral reflectance differences vs SeaWiFS AOD anomaly relative to AERONET. These scatter-density plots show the difference between SeaWiFS-derived ocean surface reflectance when the AOD used for atmospheric correction is the baseline SeaDAS value vs when the AERONET value is used, as a function of SeaWiFS–AERONET AOD₄₄₀ difference. Plots for R_{rs} (sr^{-1}) at (a)–(d) 670, (e)–(h) 555, and (i)–(l) 443 nm. Plots (a), (e), (i) include all points; (b), (f), (j) show only those points assigned to fine-dominated aerosol; (c), (g), (k) show only dust; and (d), (h), (l) only maritime aerosol, respectively, based on the same proxy criteria used for Fig. 4.

to specify quantitative adjustments to the R_{rs} retrieval process itself, one would also like to compare the retrieved R_{rs} values with coincident in situ observations. For this application, in situ ocean color data, coincident with SeaWiFS observations, also need to be collocated with at least sun photometer AOD measurements, and they should be sufficiently well sampled to allow for meaningful stratification by AOD and aerosol type. Normally viewed ocean surface water-leaving radiance (nL_w) along with AERONET direct-sun AOD measurements have been collected at several AERONET-OC stations (e.g., Zibordi et al. 2009). We searched the AERONET-OC database, applying the selection criteria of 1) SeaWiFS observations within 5-km radial proximity to the AERONET-OC site to reduce scene heterogeneity effects and 2) ± 30 min of SeaWiFS overpass for AERONET to limit atmospheric variability. At the Venice station (this is the AERONET-OC

name for the site at Venice, adopted here for consistency), 234 points that meet the selection criteria were obtained, 41 at Gustav Dalen Tower, and none at CERES Ocean Validation Experiment (COVE) or Martha's Vineyard Coastal Observatory (MVCO). Loosening these criteria significantly increases the scatter among the points but does not change the observed patterns, and by far the majority of coincident measurements overall were taken at Venice. However, neither atmospheric nor surface conditions at Venice are typical of much of the world's oceans or seas, an additional limitation of the data currently available for this type of exercise.

Note that there are some differences between the data volume in this analysis and that available on the NASA online SeaWiFS Bio-optical Archive and Storage System (SeaBASS) validation matchup data search (<http://seabass.gsfc.nasa.gov/seabasscgi/search.cgi>). Overall, SeaBASS

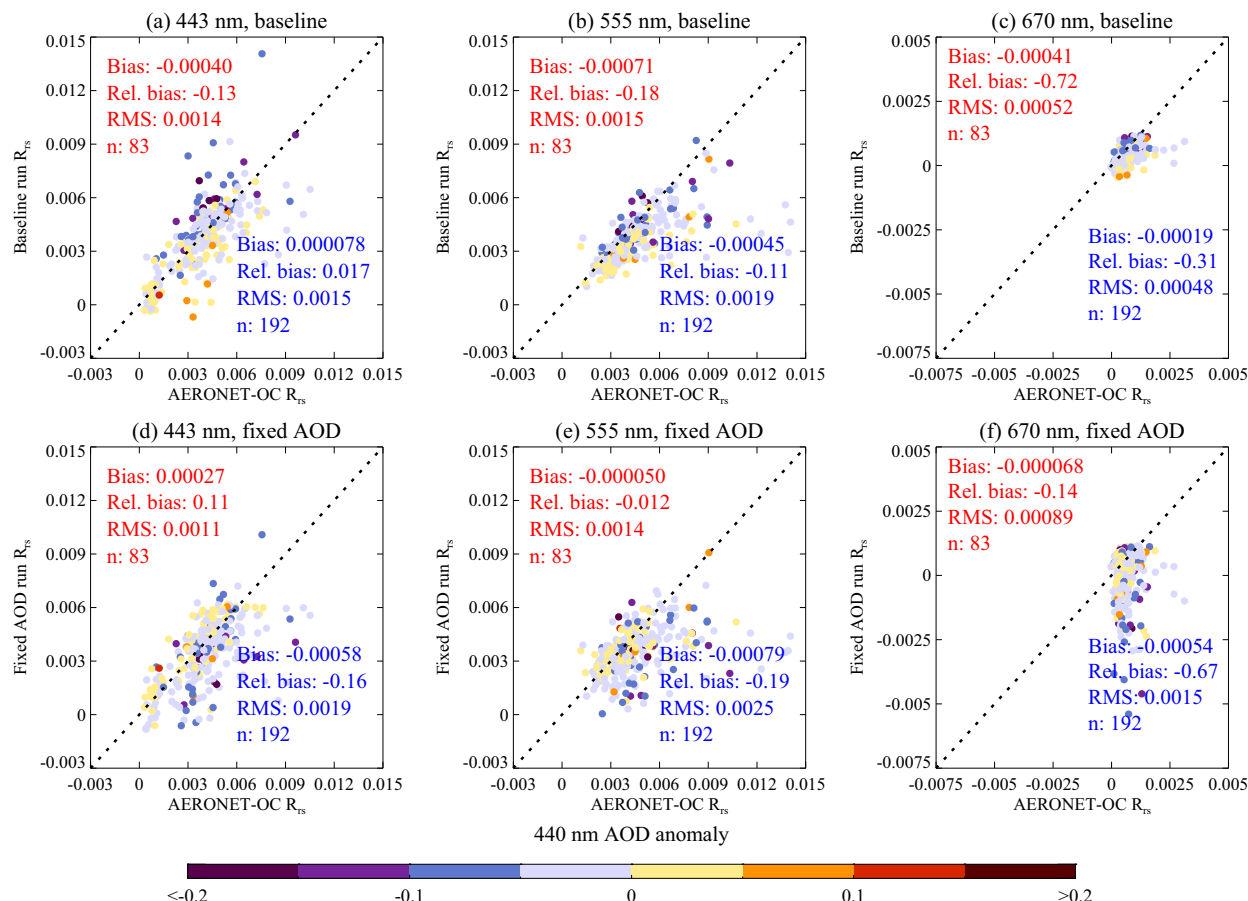


FIG. 9. Scatterplots showing coincident SeaWiFS vs in situ R_{rs} observations, specifically: [(baseline or fixed) R_{rs}] vs [AERONET-OC R_{rs}]. Plots are presented for 443 (left column), 555 (middle column), and 670 nm (right), comparing separately the (a)–(c) baseline and (d)–(f) fixed-AOD R_{rs} values at the Venise and Gustav Dalen Tower AERONET-OC sites. The points are color-coded by (SeaWiFS – AERONET) AOD anomaly at 440 nm, and summary statistics are presented on the panels in red and blue for the subsets of points with positive and negative AOD anomalies, respectively. These statistics are median bias (sr^{-1}), median relative bias, RMS difference (sr^{-1}), and data count. The median relative bias is defined as the median bias, normalized by the AERONET-OC R_{rs} value. The point selection criteria are described in the text.

returns approximately 3 times more matchups between SeaWiFS and AERONET-OC. In both cases, the majority of matchups are for the Venise site. The differences in data volume arise from a combination of factors:

- 1) We use the global area coverage (GAC) SeaWiFS data, with a nominal pixel spacing of 4.4 km. SeaBASS uses merged local area coverage (MLAC) data, which are only available for parts of the world. But where available, these data have a pixel spacing of 1.1 km and approximately twice the swath width of the GAC data, which accounts for a factor of approximately 2 of the sampling difference.
- 2) As mentioned above, some of the OBP data quality checks cannot be applied to the fixed-AOD run, which reduces the data volume by a little under 10% on average (although it is somewhat site dependent, and is a strong factor for COVE and MVCO).
- 3) SeaBASS searches for a temporal matchup between SeaWiFS and AERONET-OC within ± 3 h. We use ± 30 min, because AOD can vary significantly over a 6-h window, particularly for high-AOD cases, so the AERONET fixed-AOD run results might not accurately represent the aerosol loading at the time of the AERONET-OC nL_w observation. By selecting only more direct matchups, we decrease the potential confounding factor of aerosol temporal variability.

This combination of factors accounts for the decrease in data volume at all sites, including the loss of all points at the COVE and MVCO stations, which are especially affected by the change in available SeaWiFS quality assurance tests.

Figure 9 compares the AERONET-OC values of R_{rs} with SeaWiFS at three wavelengths for both the baseline (top row) and fixed-AOD (bottom row) runs, for the

available combination of data from Venice and Gustav Dalen Tower. For these plots, in situ R_{rs} was calculated from the nL_w data provided by AERONET-OC, including correction for bidirectional reflectance according to Morel et al. (2002). Statistics are provided, calculated separately for cases of positive and negative AOD₄₄₀ anomalies, as these subsets exhibit contrasting behavior.

For points having positive AOD anomalies (around a third of cases in this sample), the fixed-AOD run shows improvements in retrieved R_{rs} bias and RMS difference relative to AERONET-OC for all three wavelengths examined except at 670 nm, where the bias improves but the RMS difference degrades. The absolute improvement in RMS difference is largest at 443 nm (0.0014–0.0011), which is also the wavelength at which the atmospheric contribution to the TOA signal arising from aerosols is typically largest.

These positive AOD anomalies are, on a global basis, found most often in low-AOD conditions, and they constitute the bulk of the global dataset (Figs. 2–4). This result thus provides direct evidence that improving the quality of aerosol information improves the quality of the atmospheric correction in this regime.

Although the vast majority of overocean cases globally would be in the low-AOD, positive AOD anomaly regime, the majority of data points in the available AERONET-OC dataset come from the Venice site, which is atypical of global aerosol conditions. For those cases showing negative AOD anomalies (blue points plotted in Fig. 9), the fixed-AOD run produced poorer results than the baseline run: specifically, R_{rs} becomes more strongly underestimated. The SeaWiFS algorithm, with the nominal atmospheric correction applied, is tuned to retrieval conditions at the Lanai site (see section 1 above), where nonabsorbing, spectrally neutral “marine” aerosols dominate. This atmospheric correction also accounts to some extent for residual glint, and for whitecap, cirrus, and subpixel cloud contributions that also tend to be spectrally neutral in the visible and NIR. So perturbing the AOD, even if it more accurately represents the atmospheric opacity, can skew the results, especially when the AOD is high. The effects of using a retrieval algorithm tuned to baseline conditions could also account for the 670-nm RMS error degradation in the fixed-AOD results at low AOD, especially as the R_{rs} dynamic range is very small at this wavelength. At locations and times when aerosols are present that absorb and scatter in a manner that is not spectrally neutral, such as dust, smoke, and some pollution particles (Dubovik et al. 2002; Russell et al. 2010), the nominal empirical relationship used for ocean color retrieval will not apply. As reviewed in section 1 above, individual dust and volcanic ash case studies, for example, show significant anomalies (e.g., Li et al.

2003; Nobileau and Antoine 2005; Porter and Nielsen 2002; Schollaert et al. 2003).

Additionally, although the fixed-AOD run set the total AOD to match AERONET values, the other aerosol properties (i.e., size/shape distribution, SSA) could not be constrained due to a lack of available data to do so. Negative AOD anomalies were most often encountered for high-AOD cases, at which these assumptions become more important. As there is some indication that the aerosol models used in SeaWiFS processing may not encompass the range of variability of aerosol optical properties in high-AOD situations (e.g., Figs. 6 and 7), the AOD anomalies in these cases could be counteracting the deficiencies in the aerosol optical models used in the retrieval. Thus, when the AOD is corrected, the R_{rs} comparison becomes worse in cases where this compensating bias is removed; this points to the need for improved capabilities for identifying aerosol “type”—specifically, appropriate optical properties—to obtain unbiased atmospheric correction as well as unbiased ocean color retrievals under the full range of conditions of interest.

In section 1 we summarize places where smoke and dust are present, and the AOD over ocean from such sources is discussed at the end of the next section. The in situ AERONET-OC observations are taken elsewhere and are very sparse, so we are not able to test these situations with available data from this source, and must rely on the much larger and more diverse SeaWiFS–AERONET dataset to further investigate the impact of different aerosol types on ocean color retrieval results.

c. Implications for atmospheric correction anomaly impacts on ocean color products

In this section, we explore the sensitivity of the derived chlorophyll-*a* concentration (Chl) to the aerosol-related R_{rs} anomalies identified in previous sections, to the extent possible with available data. The operational SeaWiFS Chl retrieval uses the ocean chlorophyll 4 (OC4) algorithm (O’Reilly et al. 1998), which is an empirical formula based on the maximum R_{rs} ratio among three blue/green bands to the 555-nm band. Essentially, as Chl increases, R_{rs} in blue bands tends to decrease, whereas R_{rs} in green bands is either reasonably invariant (510 nm) or tends to increase (555 nm). Chl is calculated as follows:

$$R = \max[R_{rs}(443, 490, 510)]/R_{rs}(555), \quad (1a)$$

$$\chi = \log_{10}(R), \quad (1b)$$

$$\text{Chl} = 10^{\{a_0 + a_1\chi + a_2\chi^2 + a_3\chi^3 + a_4\chi^4\}}. \quad (1c)$$

The a_i values are coefficients determined from a reference training dataset. The two upper rows of Fig. 10

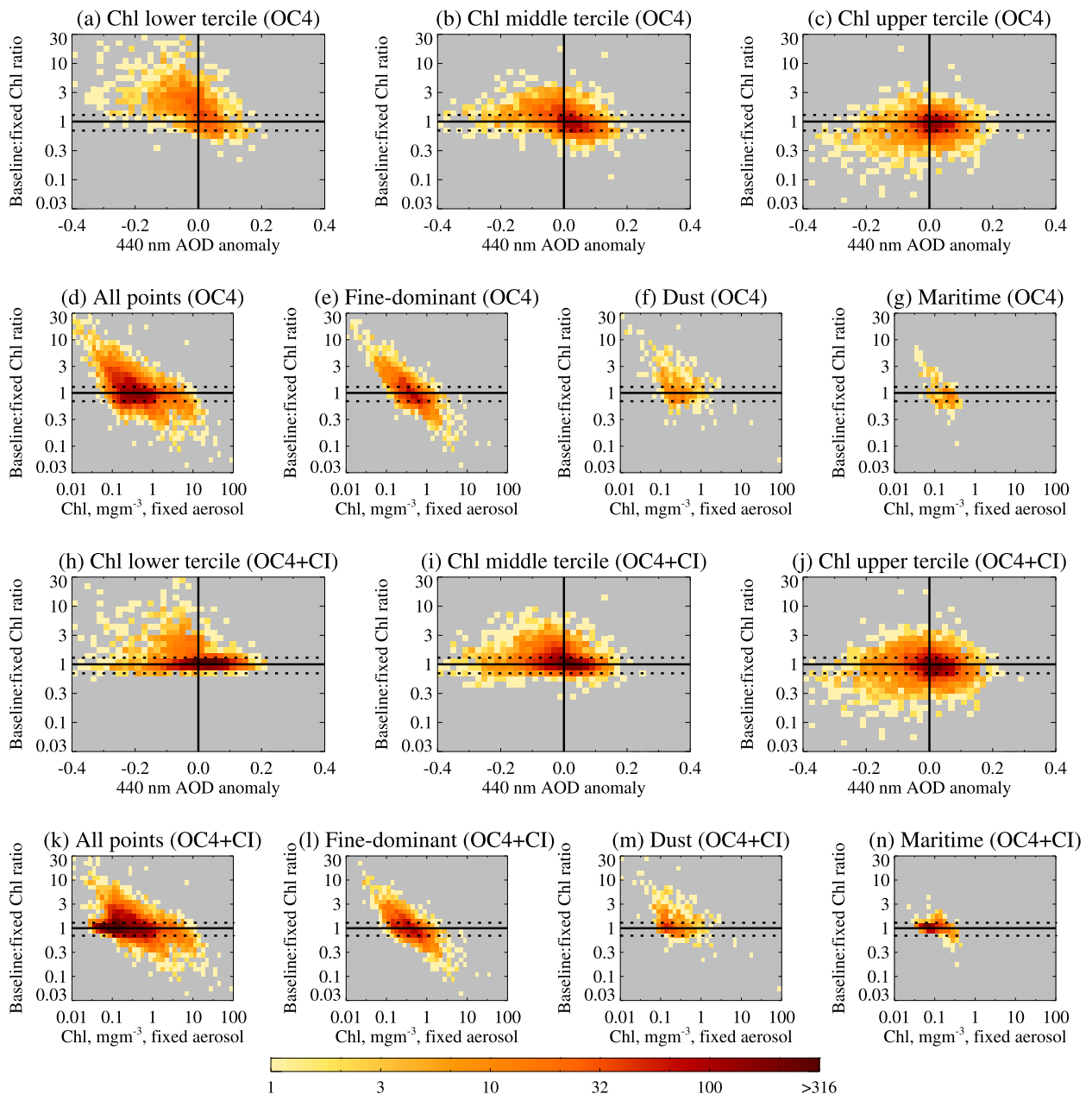


FIG. 10. (a)–(g) Difference-density plots showing ratio of chlorophyll-*a* concentrations for the baseline SeaWiFS algorithm to the corresponding AERONET-fixed-AOD values (*y* axis) vs the associated baseline SeaWiFS AOD anomaly relative to AERONET (*x* axis; row 1), and vs the associated chlorophyll-*a* concentration value for the fixed-AOD run (row 2). The row 1 plots are stratified by chlorophyll-*a* concentration values, partitioned so each plot contains roughly equal numbers of points: (a) <0.171 ; (b) 0.171 and 0.433 ; (c) $>0.433 \text{ mg m}^{-3}$. The row 2 plots are stratified by aerosol type, based on the proxies used for Figs. 4 and 5: (d) all points in the dataset; (e) only fine-mode points; (f) only points for the dusty sites; and (g) only maritime sites. (h)–(n) As in (a)–(g), except the advanced CI algorithm was used, and the tertile divisions here are at (h) <0.116 ; (i) 0.116 and 0.259 ; (j) $>0.259 \text{ mg m}^{-3}$. Note that the vertical scales on all these plots, and the horizontal scales for the plots of rows 2 and 4, are logarithmic. The bounds of the nominal $\sim 30\%$ uncertainty of the OC4 algorithm are shown as horizontal dashed lines.

show how the SeaWiFS-retrieved Chl differs between the baseline and fixed-AOD runs, as a function of the AOD anomaly relative to AERONET in row 1, and as a function of SeaWiFS-retrieved Chl (from the OC4

algorithm) in row 2. The row 1 data are stratified by chlorophyll-*a* concentration into three groupings having equal numbers of points, and the row 2 data are segregated by aerosol type, based on the same proxies used

for Figs. 4 and 5. Figure 10 also shows the bounds of the nominal $\sim 30\%$ uncertainty of the OC4 algorithm (which is based on the scatter in the training dataset used to derive the coefficients), as horizontal dashed lines.

For the middle ($0.171 < \text{Chl} < 0.433 \text{ mg m}^{-3}$) and upper ($\text{Chl} > 0.433 \text{ mg m}^{-3}$) terciles (Figs. 10b and 10c), the bulk of the Chl values lie within the nominal uncertainty limits, without significant dependence on the AOD anomaly; that is, the change introduced by the atmospheric correction anomaly is smaller than the basic uncertainty in the OC4 relationship. This is likely because errors in R_{rs} are spectrally correlated (Fig. 8), such that the ratio method of OC4 [Eq. (1)] compensates, within the stated uncertainty, for these differences. For the lower ($\text{Chl} < 0.171 \text{ mg m}^{-3}$) tercile, a negative AOD anomaly is more strongly correlated with an overestimate of Chl (and conversely), indicating that the OC4 method is much more sensitive to these R_{rs} differences. The second row of Fig. 10 shows a pattern suggesting that atmospheric correction anomalies might dampen the dynamic range of the retrieved Chl, in that it is overestimated toward the lower end of the range and underestimated toward the upper end. The shapes of the point clouds in these panels are consistent among all the aerosol-type groupings.

Recall that chlorophyll-*a* concentration is determined based on phytoplankton absorption in the 440-nm spectral region. When AOD is underestimated, which occurs primarily at high AOD (Figs. 2 and 3), and correspondingly, R_{rs} tends to be overestimated (Fig. 8), we might on physical grounds expect Chl to be underestimated. However, the baseline Chl appears higher at low concentrations primarily when the AOD anomaly is negative (Fig. 10a); that is, when the AOD of the baseline case is low relative to AERONET, the baseline-retrieved Chl comes out higher than that for the AERONET-fixed-AOD situation. Further, these cases, where AOD is lower in the baseline yet the retrieved Chl value comes out systematically higher, apply at low Chl for all aerosol-type strata in Figs. 10e–g. Conversely, lower baseline Chl values tend to occur for positive AOD anomaly at low to moderate concentrations (Figs. 10a and 10b), and again appear in all aerosol-type strata in Figs. 10e–g. This reflects a subtlety in the way spectral ratios are used in the SeaWiFS algorithm to translate surface reflectance into chlorophyll-*a* concentration [i.e., Eq. (1)].

Recently, a further empirical adjustment aimed in part at mitigating atmospheric correction errors in the band-ratio (e.g., OC4) method has been developed. It uses a “color index” (CI), which is based on a line height derived from the difference between the observed green-band R_{rs} and that obtained by linearly

interpolating between blue- and red-band R_{rs} (Hu et al. 2012):

$$\text{CI} = R_{rs}(555) - \{R_{rs}(443) + (555 - 443)/(670 - 443) \times [R_{rs}(670) - R_{rs}(443)]\}, \quad (2a)$$

$$\text{Chl} = 10^{-0.4909 + 191.659 \times \text{CI}} \quad \text{for} \quad \text{CI} \leq 0.0005 \text{ sr}^{-1}. \quad (2b)$$

The CI method is considered effective primarily in oligotrophic (i.e., biologically low productivity) waters, generally away from coasts, where Chl values are typically $\leq 0.25 \text{ mg m}^{-3}$. It is expected to become the standard algorithm in a recent update to the SeaWiFS standard products, as it is now for MODIS.

The lower two rows of Fig. 10 are equivalent to the upper two rows, except using a weighted combination of the OC4 and CI methods, as described in Hu et al. (2012). As a result of the change in Chl, the tercile ranges adjust slightly (breakpoints of 0.116 and 0.259 mg m^{-3} , respectively). Comparing the upper and lower two rows, it is clear that the points in the lower (and, to a lesser extent, middle) tercile lie closer to the 1:1 ratio line, indicating that the OC4 + CI method is less sensitive than OC4 alone to atmospheric correction anomalies in this regime. However, the lower tercile retains a population of points with a negative AOD anomaly and Chl overestimate, and the dampening of the dynamic range seen in OC4 (Figs. 10d–g) is still present in the combination OC4 + CI (Figs. 10k–n). Overall for Fig. 10, relative to the Chl values from the fixed-AOD method, the OC4 data are higher than the 30% uncertainty envelope about 17% of the time and lower about 9% of the time. The Hu et al. (2012) data (OC4 + CI) are higher 22% of the time and lower 9% of the time.

In summary, it is clear from Figs. 8–10 that the AOD, and possibly also the SSA, adopted in the ocean color atmospheric correction has an impact on the derived products. Chl is less strongly affected than R_{rs} over much of the parameter space, due to the way the spectral correlation of R_{rs} anomalies interacts with the form of the OC4 and CI algorithms. For the proxies associated with some absorbing and coarse-mode aerosol populations, the differences shown in these figures persist and are likely to skew the results, but the validation data required to directly test the impact of these species on derived ocean color variables more generally are as yet lacking.

We conclude this section by looking more broadly at locations where issues with R_{rs} and possibly with the resultant chlorophyll-*a* concentration, might preferentially occur, globally. The cases studied here are all

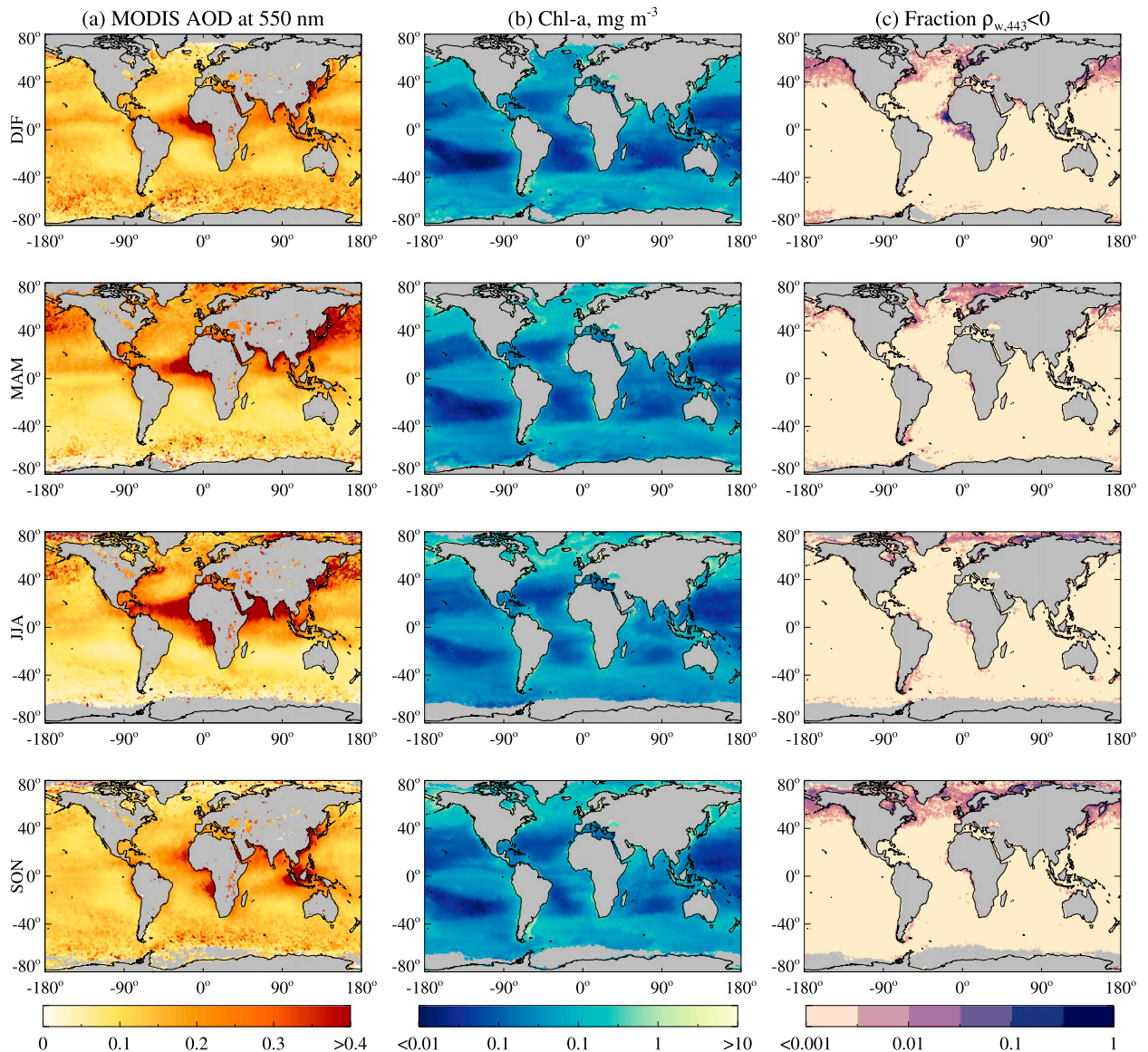


FIG. 11. Global map showing MODIS Collection 6 overocean AOD at 550 nm (column a), SeaWiFS-retrieved chlorophyll-*a* concentration, with individual points averaged in log space (column b), and fraction of all retrievals where the SeaWiFS algorithm identified negative $L_{w,443}$ (column c). All variables are plotted at 1° resolution, for four 3-month periods covering 2006 (top–bottom rows) DJF, MAM, JJA, and SON; columns b and c are plotted with logarithmic scales.

ones that passed the SeaWiFS algorithm acceptance criteria. Where the derived L_w is negative or the derived Chl value exceeds the 100 mg m^{-3} algorithm upper bound, one possibility is that the estimated aerosol contribution to the TOA reflectance might be overestimated, whereas when the derived Chl is $< 0.01 \text{ mg m}^{-3}$, it is possible that the aerosol contribution is underestimated. (Note that although this is applied as an algorithm acceptance criterion, having $\text{Chl} > 100 \text{ mg m}^{-3}$ is possible in nature, especially in nutrient-rich coastal waters.)

Figure 11 shows the 2006 global seasonal distributions of MODIS-derived AOD_{550} (column a), from the new MODIS *Aqua* Collection 6 reprocessing (Levy et al. 2013), SeaWiFS-retrieved chlorophyll-*a* concentration (column b) and a fraction of cases where the SeaWiFS algorithm produces negative L_w (column c). The retrieved Chl rarely exceeds the upper limit (not shown), except in some inland waters and at high northern latitudes in the Greenland Sea and Norwegian Sea regions in spring and autumn, where AOD is generally low. However, the more extreme situation of underestimated

retrieved L_w , where its value is actually negative, occurs 1) off west-equatorial Africa, with a seasonal cycle that peaks in northern winter and shows a less prominent peak in northern summer; 2) in the North Pacific and to some extent in the North Atlantic from September through February; and 3) again in the Greenland, Norwegian, and Barents Seas, with a peak in northern spring. As such, the African biomass-burning AOD maxima and the peaks in negative L_w values might be related, and possibly also the springtime AOD and L_w peaks in the Greenland Sea and Norwegian Sea regions.

Note that the level of aggregation needs to be considered when interpreting column c of Fig. 11. For example, in the Atlantic region off northwest Africa, the AOD is in the “moderate” range *most* of the time when ocean color values are retrieved, as major smoke and dust plumes will be rejected by the SeaWiFS algorithm. In such cases, AOD is more likely to be overestimated based on Fig. 4, consistent with an underestimated R_{rs} at 443 nm that might go negative (Fig. 8). Generally, atmospheric correction anomalies are more likely to be significant where AOD is typically higher and more variable and where ocean biological activity tends to be greatest, such as near coasts and along major aerosol transport pathways. These are also among the most important places where ocean color products are needed for carbon cycle and other environmental studies.

4. Conclusions

Even in relatively homogeneous offshore waters, separating the contributions to R_{rs} of phytoplankton absorption, colored dissolved organic matter (CDOM), and suspended particles within the water from remote sensing signals is an extremely challenging empirical endeavor (e.g., Siegel et al. 2013). As such, identifying the additional effects of dust, smoke, and other airborne particles that exhibit wavelength-dependent absorption and scattering is needed for the quantitative interpretation of space-based spectral observations in terms of ocean color, especially along the transport pathways, where these aerosols are common.

We used over 13 000 coincident SeaWiFS–AERONET observations to assess statistically the sign and magnitude of AOD anomalies in the SeaWiFS atmospheric correction process, and correlated those with the derived water-leaving reflectances and chlorophyll-*a* concentrations in the SeaWiFS standard OBP ocean color retrieval product. We also used several proxy indicators to separate, at least qualitatively, the likely effect of different aerosol types (e.g., different particle sizes and SSAs) on these patterns. We show that the atmospheric correction

applied to the SeaWiFS data tends to overestimate AOD₄₄₀ on order 0.02 in the low-AOD regime, where AOD₈₇₀ is less than about 0.15, but increasingly underestimates AOD₄₄₀ at higher aerosol opacity (Fig. 2), and overestimates SSA₄₄₀ wherever its value falls below about 0.96 (Fig. 7). Also, the AOD spectral slope is systematically underestimated for coarse-mode-dominated aerosol types (i.e., for Ångström exponent < 0.8). As such, *aerosol-type-dependent* anomalies tend to occur for both AOD and its spectral dependence. To explore the sensitivity of the derived surface reflectance and chlorophyll-*a* concentration to the spectral AODs adopted for atmospheric correction, we compared the results from a nominal run of the SeaWiFS algorithm and one where the AOD was fixed to the corresponding value obtained by AERONET sun photometers. For the AERONET-constrained run, particle microphysical properties were also selected to match the corresponding AERONET ANG and the ambient RH as closely as possible within the 80 aerosol models in the SeaWiFS algorithm. We find that the AOD anomaly patterns are reflected in the retrieved R_{rs} values. As might be expected, atmospheric correction AOD overestimation and underestimation produce R_{rs} that is systematically lower and higher, respectively, and the differences are correlated across the spectral range (Fig. 8). Retrieved R_{rs} values also show sensitivity to aerosol-type proxy, though correlations with SSA anomalies specifically in the atmospheric correction algorithm are too subtle to be quantified here.

The availability of correlative data to examine directly the effect of improved atmospheric correction on the ocean color data products is limited. However, we confirm that for the low-AOD regime, comprising the bulk of the open ocean, modest improvement in the blue R_{rs} retrievals appears to be achieved, compared to the in situ observations, when the AOD is constrained by AERONET values (Fig. 9). For higher AOD conditions, however, correcting only the AOD to coincident ground truth observations leads to poorer comparison with in situ R_{rs} data, likely at least in part due to aerosol optical models in the SeaWiFS operational processing that do not encompass the range of aerosol types found in these cases. Thus, as demonstrated by previous individual case studies for which validation data were available, when absorbing aerosol, such as dust, smoke, or some pollution particles, are present, retrieved ocean color variables are aliased by spectral AOD and possibly also SSA anomalies in the atmospheric correction.

Although L_w or R_{rs} is used to derive an entire suite of ocean color data products, we also analyzed the sensitivity of retrieved chlorophyll-*a* concentration to AOD, as Chl is probably the most widely used biophysical ocean product from SeaWiFS and MODIS. By comparing

results from the proposed SeaWiFS OC4 + CI algorithm, run with AOD constrained by coincident AERONET measurements, with results from the nominal algorithm run, we find that the resulting R_{rs} anomaly pattern is also reflected in the derived Chl values, though in a more complex way than the AOD- R_{rs} relationship itself. AOD adjustments affect the retrieved Chl values most frequently toward the high and low ends of the Chl distribution (Fig. 10, rows 1 and 2). The SeaWiFS OC4 + CI algorithm, which is now the SeaWiFS version R2014.0 standard Chl product algorithm, generates a qualitatively similar reduction in Chl dynamic range due to the AOD perturbations but of smaller magnitude than for OC4 alone; that is, the proposed algorithm has lower sensitivity to AOD (Fig. 10, rows 3 and 4; Hu et al. 2012).

Comparisons between satellite R_{rs} observations and coincident surface-based spectral AOD and in situ R_{rs} values can contribute a great deal toward refining ocean color retrieval algorithms, and would elevate the R_{rs} and Chl sensitivity studies performed here to validation analyses of existing ocean color products. However, available in situ data are insufficient to stratify by AOD, aerosol-type proxies, and possibly other environmental factors for deeper analysis regarding aerosol amount and type, which is the focus of the current study. Acquiring statistically well-sampled datasets for atmospheric correction validation, including coincident AOD, aerosol type (i.e., particle size distribution, shape, SSA), and R_{rs} or L_w data, especially where absorbing dust, smoke, or pollution particles are present, would make an important contribution to ongoing and future satellite ocean color missions.

It is a quantitative question as to when and where particular atmospheric correction constraints are needed to retrieve different ocean surface parameters from measured TOA radiances in specific spectral bands. AOD and aerosol-type constraint requirements are likely to be greater for planned future missions, such as NASA's Pre-Aerosol, Clouds, and Ocean Ecosystem (PACE) mission, which aims to retrieve ocean color parameters at wavelengths even shorter than 412 nm. AOD is generally higher at shorter wavelengths, and spectral extrapolation of assumed aerosol optical properties might need to be performed over a larger spectral range than is done for current and historical sensors such as SeaWiFS and MODIS. In addition, some of the most biologically productive waters occur near coasts and along major aerosol transport pathways, where AOD tends to be higher; where absorbing aerosols, such as desert dust, wildfire smoke, or pollution particles, can dominate; and where aerosol fertilization can contribute to ocean productivity.

Acknowledgments. We thank NASA's Ocean Biology Processing Group for maintaining the SeaWiFS record and for providing level 1 and ancillary data, and the SeaDAS software; Christopher Proctor of the OBPB for help to access and interpret the AERONET-OC in situ data; Brent Holben and the AERONET scientists, site PIs, and site managers; and Giuseppe Zibordi and the AERONET-OC scientists, site PIs, and site managers, for the AERONET and AERONET-OC datasets used in this study (available from <http://aeronet.gsfc.nasa.gov>). We also thank Steve Massie and two anonymous reviewers for their comments and suggestions, which improved the paper. The work of R. Kahn on this study is supported in part by NASA's Climate and Radiation Research and Analysis Program under H. Maring, NASA's Atmospheric Composition Program under R. Eckman, and the NASA Aerosol-Cloud-Ecosystem (ACE) project's science definition effort.

REFERENCES

- Ahmad, Z., B. A. Franz, C. R. McClain, E. J. Kwiatkowska, J. Werdell, E. P. Shettle, and B. N. Holben, 2010: New aerosol models for the retrieval of aerosol optical thickness and normalized water-leaving radiances from the SeaWiFS and MODIS sensors over coastal regions and open oceans. *Appl. Opt.*, **49**, 5545–5560, doi:[10.1364/AO.49.005545](https://doi.org/10.1364/AO.49.005545).
- Antoine, D., and D. Nobileau, 2006: Recent increase in Saharan dust transport over the Mediterranean Sea, as revealed by ocean color satellite (SeaWiFS) observations. *J. Geophys. Res.*, **111**, D12214, doi:[10.1029/2005JD006795](https://doi.org/10.1029/2005JD006795).
- Aznay, O., R. Santer, and F. Zagolski, 2014: Validation of atmospheric scattering functions used in atmospheric correction over the ocean. *Int. J. Remote Sens.*, **35**, 4984–5003, doi:[10.1080/01431161.2014.933282](https://doi.org/10.1080/01431161.2014.933282).
- Clark, D. K., H. R. Gordon, K. J. Voss, Y. Ge, W. Broenkow, and C. Trees, 1997: Validation of atmospheric correction over the oceans. *J. Geophys. Res.*, **102**, 17 209–17 217, doi:[10.1029/96JD03345](https://doi.org/10.1029/96JD03345).
- Colarco, P. R., R. A. Kahn, L. A. Remer, and R. C. Levy, 2014: Impact of satellite viewing-swath width on global and regional aerosol optical thickness statistics and trends. *Atmos. Meas. Tech.*, **7**, 2313–2335, doi:[10.5194/amt-7-2313-2014](https://doi.org/10.5194/amt-7-2313-2014).
- Dubovik, O., and M. D. King, 2000: A flexible inversion algorithm for retrieval of aerosol optical properties from Sun and sky radiance measurements. *J. Geophys. Res.*, **105**, 20 673–20 696, doi:[10.1029/2000JD900282](https://doi.org/10.1029/2000JD900282).
- , A. Smirnov, B. N. Holben, M. D. King, Y. J. Kaufman, T. F. Eck, and I. Slutsker, 2000: Accuracy assessment of aerosol optical properties retrieval from AERONET sun and sky radiance measurements. *J. Geophys. Res.*, **105**, 9791–9806, doi:[10.1029/2000JD900040](https://doi.org/10.1029/2000JD900040).
- , B. Holben, T. F. Eck, A. Smirnov, Y. J. Kaufman, M. D. King, D. Tanre, and I. Slutsker, 2002: Variability of absorption and optical properties of key aerosol types observed in worldwide locations. *J. Atmos. Sci.*, **59**, 590–608, doi:[10.1175/1520-0469\(2002\)059<0590:VOAAOP>2.0.CO;2](https://doi.org/10.1175/1520-0469(2002)059<0590:VOAAOP>2.0.CO;2).
- Eck, T. F., B. N. Holben, J. S. Reid, O. Dubovik, A. Smirnov, N. T. O'Neill, I. Slutsker, and S. Kinne, 1999: Wavelength dependence

- of the optical depth of biomass burning, urban, and desert dust aerosols. *J. Geophys. Res.*, **104**, 31 333–31 349, doi:[10.1029/1999JD900923](https://doi.org/10.1029/1999JD900923).
- , and Coauthors, 2003: High aerosol optical depth biomass burning events: A comparison of optical properties for different source regions. *Geophys. Res. Lett.*, **30**, 2035, doi:[10.1029/2003GL017861](https://doi.org/10.1029/2003GL017861).
- , and Coauthors, 2005: Columnar aerosol optical properties at AERONET sites in central eastern Asia and aerosol transport to the tropical mid-Pacific. *J. Geophys. Res.*, **110**, D06202, doi:[10.1029/2004JD005274](https://doi.org/10.1029/2004JD005274).
- Esaias, W. E., and Coauthors, 1998: An overview of MODIS capabilities for ocean science observations. *IEEE Trans. Geosci. Remote Sens.*, **36**, 1250–1265, doi:[10.1109/36.701076](https://doi.org/10.1109/36.701076).
- Franz, B. A., E. J. Ainsworth, and S. Bailey, 2001: SeaWiFS vicarious calibration: An alternative approach utilizing simultaneous *in situ* observations of oceanic and atmospheric optical properties. In situ aerosol optical thickness collected by the SIMBIOS program (1997–2000): Protocols, and data QC and analysis, G. S. Fargion, R. Barnes, and C. McClain, Eds., NASA Tech. Memo. NASA/TM—2001–209982, 88–96.
- , S. W. Bailey, P. J. Werdell, and C. R. McClain, 2007: Sensor-independent approach to the vicarious calibration of satellite ocean color radiometry. *Appl. Opt.*, **46**, 5068–5082, doi:[10.1364/AO.46.005068](https://doi.org/10.1364/AO.46.005068).
- Gordon, H. R., 1997: Atmospheric correction of ocean color imagery in the Earth Observing System era. *J. Geophys. Res.*, **102**, 17 081–17 106, doi:[10.1029/96JD02443](https://doi.org/10.1029/96JD02443).
- , and M. Wang, 1994: Retrieval of water-leaving radiance and aerosol optical thickness over oceans with SeaWiFS: A preliminary algorithm. *Appl. Opt.*, **33**, 443–452, doi:[10.1364/AO.33.000443](https://doi.org/10.1364/AO.33.000443).
- He, X., D. Pan, Y. Bai, Q. Zhu, and F. Gong, 2011: Evaluation of the aerosol models for SeaWiFS and MODIS by AERONET data over open oceans. *Appl. Opt.*, **50**, 4353–4364, doi:[10.1364/AO.50.004353](https://doi.org/10.1364/AO.50.004353).
- Holben, B. N., and Coauthors, 1998: AERONET—A federated instrument network and data archive for aerosol characterization. *Remote Sens. Environ.*, **66**, 1–16, doi:[10.1016/S0034-4257\(98\)00031-5](https://doi.org/10.1016/S0034-4257(98)00031-5).
- Hu, C., Z. Lee, and B. Franz, 2012: Chlorophyll *a* algorithms for oligotrophic oceans: A novel approach based on three-band reflectance difference. *J. Geophys. Res.*, **117**, C01011, doi:[10.1029/2011JC007395](https://doi.org/10.1029/2011JC007395).
- Huang, J., C. Zhang, and J. M. Prospero, 2010: African dust outbreaks: A satellite perspective of temporal and spatial variability over the tropical Atlantic Ocean. *J. Geophys. Res.*, **115**, D05202, doi:[10.1029/2009JD012516](https://doi.org/10.1029/2009JD012516).
- Kahn, R. A., and B. J. Gaitley, 2015: An analysis of global aerosol type as retrieved by MISR. *J. Geophys. Res. Atmos.*, **120**, 4248–4281, doi:[10.1002/2015JD023322](https://doi.org/10.1002/2015JD023322).
- , P. Banerjee, D. McDonald, and D. Diner, 1998: Sensitivity of multiangle imaging to aerosol optical depth, and to pure-particle size distribution and composition over ocean. *J. Geophys. Res.*, **103**, 32 195–32 213, doi:[10.1029/98JD01752](https://doi.org/10.1029/98JD01752).
- Kalashnikova, O. V., and R. A. Kahn, 2008: Mineral dust plume evolution over the Atlantic from combined MISR/MODIS aerosol retrievals. *J. Geophys. Res.*, **113**, D24204, doi:[10.1029/2008JD010083](https://doi.org/10.1029/2008JD010083).
- Kinne, S., and Coauthors, 2006: An AeroCom initial assessment—Optical properties in aerosol component modules of global models. *Atmos. Chem. Phys.*, **6**, 1815–1834, doi:[10.5194/acp-6-1815-2006](https://doi.org/10.5194/acp-6-1815-2006).
- Levy, R. C., S. Mattoo, L. A. Munchak, L. A. Remer, A. M. Sayer, F. Patadia, and N. C. Hsu, 2013: The Collection 6 MODIS aerosol products over land and ocean. *Atmos. Meas. Tech.*, **6**, 2989–3034, doi:[10.5194/amt-6-2989-2013](https://doi.org/10.5194/amt-6-2989-2013).
- Li, L., H. Fukushima, R. Frouin, B. G. Mitchell, M.-X. He, I. Uno, T. Takamura, and S. Ohta, 2003: Influence of submicron absorptive aerosol on Sea-viewing Wide Field-of-view Sensor (SeaWiFS)-derived marine reflectance during Aerosol Characterization Experiment (ACE)-Asia. *J. Geophys. Res.*, **108**, 4472, doi:[10.1029/2002JD002776](https://doi.org/10.1029/2002JD002776).
- McCarthy, S. C., R. W. Gould Jr., J. Richman, C. Kearney, and A. Lawson, 2012: Impact of aerosol model selection on water-leaving radiance retrievals from satellite ocean color imagery. *Remote Sens.*, **4**, 3638–3665, doi:[10.3390/rs4123638](https://doi.org/10.3390/rs4123638).
- McClain, C. R., M. L. Cleave, G. C. Feldman, W. W. Gregg, S. B. Hooker, and N. Kuring, 1998: Science quality SeaWiFS data for global biosphere research. *Sea Technol.*, **39**, 10–16.
- Mélin, F., and G. Zibordi, 2010: Vicarious calibration of satellite ocean color sensors at two coastal sites. *Appl. Opt.*, **49**, 798–810, doi:[10.1364/AO.49.000798](https://doi.org/10.1364/AO.49.000798).
- , M. Clerici, G. Zibordi, B. N. Holben, and A. Smirnov, 2010: Validation of SeaWiFS and MODIS aerosol products with globally distributed AERONET data. *Remote Sens. Environ.*, **114**, 230–250, doi:[10.1016/j.rse.2009.09.003](https://doi.org/10.1016/j.rse.2009.09.003).
- , G. Zibordi, T. Carlund, B. N. Holben, and S. Stefan, 2013a: Validation of SeaWiFS and MODIS Aqua/Terra aerosol products in coastal regions of European marginal seas. *Oceanologia*, **55**, 27–51, doi:[10.5697/oc.55-1.027](https://doi.org/10.5697/oc.55-1.027).
- , —, and B. N. Holben, 2013b: Assessment of the aerosol products from the SeaWiFS and MODIS ocean-color missions. *IEEE Geosci. Remote Sens. Lett.*, **10**, 1185–1189, doi:[10.1109/LGRS.2012.2235408](https://doi.org/10.1109/LGRS.2012.2235408).
- Morel, A., and L. Prieur, 1977: Analysis of variations in ocean color. *Limnol. Oceanogr.*, **22**, 709–722, doi:[10.4319/lo.1977.22.4.0709](https://doi.org/10.4319/lo.1977.22.4.0709).
- , D. Antoine, and B. Gentili, 2002: Bidirectional reflectance of oceanic waters: Accounting for Raman emission and varying particle scattering phase function. *Appl. Opt.*, **41**, 6289–6306, doi:[10.1364/AO.41.006289](https://doi.org/10.1364/AO.41.006289).
- Nobileau, D., and D. Antoine, 2005: Detection of blue-absorbing aerosols using near-infrared and visible (ocean color) remote sensing observations. *Remote Sens. Environ.*, **95**, 368–397, doi:[10.1016/j.rse.2004.12.020](https://doi.org/10.1016/j.rse.2004.12.020).
- O'Reilly, J. E., S. Maritorena, B. G. Mitchell, D. A. Siegel, K. L. Carder, S. A. Garver, M. Kahru, and C. McClain, 1998: Ocean color chlorophyll algorithms for SeaWiFS. *J. Geophys. Res.*, **103**, 24 937–24 953, doi:[10.1029/98JC02160](https://doi.org/10.1029/98JC02160).
- Porter, J., and T. Nielsen, 2002: Atmospheric correction near Hawaii: Clear sky and volcano plumes. *Proc. Sixth Pan Ocean Remote Sensing Conf.*, Bali, Indonesia, PORSEC, 3 pp. [Available online at http://www.soest.hawaii.edu/porter/Bali_Atmos_Corr.pdf.]
- Ransibrahmanakul, V., and R. P. Stumpf, 2006: Correcting ocean colour reflectance for absorbing aerosols. *Int. J. Remote Sens.*, **27**, 1759–1774, doi:[10.1080/01431160500380604](https://doi.org/10.1080/01431160500380604).
- Remer, L. A., and Coauthors, 2008: Global aerosol climatology from the MODIS satellite sensors. *J. Geophys. Res.*, **113**, D14S07, doi:[10.1029/2007JD009661](https://doi.org/10.1029/2007JD009661).
- Russell, P. B., and Coauthors, 2010: Absorption Angstrom exponent in AERONET and related data as an indicator of aerosol

- composition. *Atmos. Chem. Phys.*, **10**, 1155–1169, doi:[10.5194/acp-10-1155-2010](https://doi.org/10.5194/acp-10-1155-2010).
- Sayer, A. M., N. C. Hsu, C. Bettenhausen, Z. Ahmad, B. N. Holben, A. Smirnov, G. E. Thomas, and J. Zhang, 2012: SeaWiFS Ocean Aerosol Retrieval (SOAR): Algorithm, validation, and comparison with other data sets. *J. Geophys. Res.*, **117**, D03206, doi:[10.1029/2011JD016599](https://doi.org/10.1029/2011JD016599).
- Schollaert, S. E., J. A. Yoder, J. E. O'Reilly, and D. L. Westphal, 2003: Influence of dust and sulfate aerosols on ocean color spectra and chlorophyll *a* concentrations derived from SeaWiFS off the U.S. east coast. *J. Geophys. Res.*, **108**, 3191, doi:[10.1029/2000JC000555](https://doi.org/10.1029/2000JC000555).
- Schuster, G. L., O. Dubovik, and B. N. Holben, 2006: Angstrom exponent and bimodal aerosol size distributions. *J. Geophys. Res.*, **111**, D07207, doi:[10.1029/2005JD006328](https://doi.org/10.1029/2005JD006328).
- Siegel, D. A., and Coauthors, 2013: Regional to global assessments of phytoplankton dynamics from the SeaWiFS mission. *Remote Sens. Environ.*, **135**, 77–91, doi:[10.1016/j.rse.2013.03.025](https://doi.org/10.1016/j.rse.2013.03.025).
- Smirnov, A., B. N. Holben, T. F. Eck, O. Dubovik, and I. Slutsker, 2000: Cloud-screening and quality control algorithms for the AERONET database. *Remote Sens. Environ.*, **73**, 337–349, doi:[10.1016/S0034-4257\(00\)00109-7](https://doi.org/10.1016/S0034-4257(00)00109-7).
- , —, Y. J. Kaufman, O. Dubovik, T. F. Eck, I. Slutsker, C. Pietras, and R. Halthore, 2002: Optical properties of atmospheric aerosol in maritime environments. *J. Atmos. Sci.*, **59**, 501–523, doi:[10.1175/1520-0469\(2002\)059<0501:OPOAAI>2.0.CO;2](https://doi.org/10.1175/1520-0469(2002)059<0501:OPOAAI>2.0.CO;2).
- , and Coauthors, 2011: Maritime aerosol network as a component of AERONET—First results and comparison with global aerosol models and satellite retrievals. *Atmos. Meas. Tech.*, **4**, 583–597, doi:[10.5194/amt-4-583-2011](https://doi.org/10.5194/amt-4-583-2011).
- Sokolik, I. N., and O. B. Toon, 1999: Incorporation of mineralogical composition into models of the radiative properties of mineral aerosol from UV to IR wavelengths. *J. Geophys. Res.*, **104**, 9423–9444, doi:[10.1029/1998JD200048](https://doi.org/10.1029/1998JD200048).
- Wang, M., Ed., 2010: Atmospheric correction for remotely-sensed ocean-colour products. IOCCG Report Series 10, 78 pp.
- Zibordi, G., and Coauthors, 2009: AERONET-OC: A network for the validation of ocean color primary products. *J. Atmos. Oceanic Technol.*, **26**, 1634–1651, doi:[10.1175/2009JTECHO654.1](https://doi.org/10.1175/2009JTECHO654.1).